This is a preprint, the final version is subject to change, of the American Mineralogist (MSA)
Cite as Authors (Year) Title. American Mineralogist, in press.
(DOI will not work until issue is live.) DOI: http://dx.doi.org/10.2138/am-2017-6063

Revision 2

Trace element zoning in hornblende: tracking and modeling the crystallization of a calc-alkaline arc pluton

CALVIN G. BARNES[1]*, RYAN BERRY[1], MELANIE A. BARNES[1], W.G. ERNST[2]

[1]Department of Geosciences, Texas Tech Univ., Lubbock, Texas 79409-1053, USA
[2]W. G. Ernst, Department of Geological Sciences, Stanford Univ., Stanford, California 94305-2115, USA

*E-mail: cal.barnes@ttu.edu

ABSTRACT

Recent studies of arc volcanic systems have shown that major and trace element zoning in calcic amphibole yields information about magmatic processes such as fractional crystallization and mixing. Similar studies of plutonic amphibole are scant, yet hold the potential to yield comparable information. To that end, calcic amphibole from late-stage rocks of the English Peak plutonic complex (EPC; Klamath Mountains, northern California) was analyzed in situ, in textural context. The pluton's late stage consists of three nested intrusive units inwardly zoned from tonalite to granite. Bulk-rock compositions and U-Pb (zircon) ages are consistent either with internal fractional crystallization of a single magma batch or with episodic emplacement of successively evolved magmas, ± magma mixing. Major and trace element abundances and zoning patterns in hornblende (s.l.) are used to test these two interpretations, identify specific magmatic units, determine the temperature range of hornblende stability, and model magma

This is a preprint, the final version is subject to change, of the American Mineralogist (MSA)
Cite as Authors (Year) Title. American Mineralogist, in press.
(DOI will not work until issue is live.) DOI: http://dx.doi.org/10.2138/am-2017-6063

crystallization. In each mapped unit, euhedral to subhedral hornblende displays prominent olive-brown core zones which crystallized at 880–775°C. Cores are embayed and rimmed by green hornblende crystallized from 775–690°C. These distinctions are preserved even in samples with moderate deuteric alteration. Some trace elements (Zr, Hf, Sr, Ti, V) decrease monotonically from core to rim, suggesting co-precipitation of hornblende with plagioclase, ilmenite, and zircon. Others (Ba, Rb) are approximately constant in highest-T core zones, then decrease, consistent with onset of biotite crystallization. In contrast, initial rim-ward decreases in Sc, Y, and REE change to near-constant values within olive-brown cores, a change modeled by a decrease in bulk partition coefficients (D) due to onset of biotite crystallization. These elements then increase in abundance in green rims, with as much as a 4-fold enrichment. Such enrichments can result from resorption/re-precipitation attending changing P and T during final emplacement, whereby trace elements in core zones were redistributed to the rims. Although hornblende compositions from the three zones are similar, outer-zone hornblende has higher Ti, Ba, Sc, and REE, whereas interior-zone hornblende has higher Mn. These differences are consistent with episodic ascent of compositionally similar but not identical magmas from a mid-crustal reservoir. Evidence for in-situ magma mixing is lacking in hornblende. Core-to-rim decrease in Zr indicates hornblende and zircon crystallized together, at T as high as 880°C. Because zircon saturation thermometry yields T estimates <720°C for all EPC samples, many of the analyzed rocks are inferred to be cumulates. This study illustrates the utility of detailed major and trace element analysis of hornblende as a means to identify magmatic units and model petrogenetic processes in calc-alkaline granitic rocks.

Keywords: Hornblende, trace element zoning, granite petrogenesis, calc-alkaline.

Always consult and cite the final, published document. See http:/www.minsocam.org or GeoscienceWorld

INTRODUCTION

A primary goal of studies of granitic systems is to characterize the petrologic evolution of magma and melt compositions as a function of pressure (P), temperature (T), and degree of crystallization. Such investigations have traditionally relied on bulk-rock geochemical data, including major and trace element compositions as well as radiogenic and stable isotope ratios. The common implicit assumption is that bulk-rock compositions represent, or at least closely reflect, magma compositions. Recent studies, particularly those focused on andesitic through rhyolitic rocks, have concluded that many magmas carry a ‘crystal cargo’ that may contain minerals from a variety of sources (e.g., Bachmann and Bergantz, 2004; Hildreth, 2004; Davidson et al., 2005; Memeti et al., 2010; Zhang et al., 2015; many others). Among many possibilities, these crystals may be (1) residual from a source region (White and Chappell, 1977; Chappell et al., 1987; Clemens et al., 2010), (2) the result of peritectic reactions of residual minerals with the host melt (Stephens, 2001; Beard et al., 2005), (3) crystals that survived mixing or assimilation events (e.g., Davidson et al., 2007, 2008; Kent, 2008; Chambefort et al., 2013; Erdmann et al., 2014), and (4) crystals that grew from the host melt at some earlier, deeper stage in the magma’s history. The potential for complex crystal loads makes petrogenetic interpretations done on the basis of bulk-rock compositions problematic, unless the principal rock-forming phases can be shown to be cognate to the magma. This problem is exacerbated by the likelihood that whatever the origins of the crystal load might have been, the bulk compositions of many plutonic rocks represent a combination of melt and accumulated crystals, and that cumulate phases may not accumulate in eutectic/cotectic proportions (e.g., Deering & Bachmann, 2010; Miller et al., 2011; Lee and Morton, 2015; Lee et al., 2015; Barnes et al., 2016a).

Significant progress in understanding the origins and significance of crystal loads has been made, particularly through analysis of ‘phenocrysts’ and melt inclusions in volcanic rocks (e.g., Bacon et al., 1992; Dunbar and Hervig, 1992; Vogel and Aines, 1996; Elburg et al, 2006; Saunders et al., 2010, many others). Fewer such studies have been applied to granitic systems (Moore and Sisson, 2008; Müller et al., 2008; Davidson et al., 2008; Dostal and Chatterjee, 2010; Memeti et al., 2010; McLeod et al., 2011; Coint et al., 2013; Barnes et al., 2016c), with the prominent exception of U-Pb, Hf, and oxygen isotopic analysis of zircon, which provides information on the timing and longevity of magmatic events and on potential magma sources and contaminants (e.g., Mattinson 2005; Coleman et al. 2004; Matzel et al. 2006; Lackey et al., 2006; Michel et al. 2008; Schaltegger et al. 2009; Shaw and Flood, 2009; Schoene et al. 2010, 2012; Tappa et al. 2011).

Although zircon microanalysis provides critical petrogenetic information, the small grain size, fine scale of compositional zoning, and difficulty in obtaining true in situ, texturally-constrained analyses (e.g., Heinonen et al., 2016) make it difficult to track evolution of an individual magma batch. An alternative approach employs major and trace element microanalysis of primary, rock-forming minerals. For example, in feldspars, zoning patterns have been used to characterize complex crystal loads (e.g., Waight et al., 2000; Davidson et al., 2001; Müller et al., 2005; Moore and Sisson, 2008; Memeti et al., 2010). However, the abundances of many petrogenetically-important trace elements in feldspars are at or below detection limits of micro-analytical methods. Alternatively, recent studies have investigated the use of trace element zoning in clinopyroxene and calcic amphibole (hereafter hornblende: Hbl) in a variety of plutonic rocks (e.g., Marks et al., 2004; Claeson et al., 2007; Turner et al., 2013; Coint et al., 2013; Kiss et al., 2014; Leuthold et al., 2014; Otamendi et al., 2016; Barnes et al., 2016c). These studies indicated that clinopyroxene and Hbl compositions provide useful monitors of compositional variation in the melt.

In this paper, we present petrographic and micro-analytical data on Hbl from the interior, late-stage granitic rocks of the English Peak pluton in northern California. We show that most Hbl crystals preserve records of compositional variation in the melt phase during crystal growth over a range of magmatic temperatures, evidence for complex crystal loads is lacking in Hbl, and changing T and/or P conditions led to surprising patterns of compatible element behavior. We also address the nature of the transition from super-solidus to sub-solidus amphibole and resultant compositional changes, and conclude that with appropriately detailed petrographic and analytical procedures, Hbl provides important insight into the evolution of plutonic magmas.

GEOLOGIC SETTING

The English Peak intrusive complex (EPC) was mapped by Seyfert (1964) and Ernst (1998) and petrologic details were presented in Schmidt (1994) and Barnes et al. (2016b). The complex is composed of three distinct intrusive masses emplaced into two Mesozoic oceanic terranes separated by a high-angle reverse fault (Fig. 1). Host rocks east of the pluton constitute the North Fork terrane, which consists of laminated metacherts and quartzofeldspathic argillites interlayered with, and overlain by metabasaltic rocks (Ernst, 1998; Scherer et al., 2010). Host rocks to the west of the pluton belong to the eastern Hayfork terrane, a chert–argillite ± greywacke mélange and broken formation with a variety of locally-derived and exotic blocks (Wright, 1982; Donato et al., 1982; Scherer et al., 2010).

Two satellite plutons represent the oldest parts of the EPC. The quartz dioritic to tonalitic Uncles Creek pluton crops out in the north and northeastern part of the complex and the gabbroic to granodioritic Heiney Bar pluton crops out in the southern part (Fig. 1). U-Pb (zircon) ages

(LA-ICPMS; Ernst et al., 2016) are 172.3 ± 2.0 Ma (Uncles Creek) and 166.9 ± 1.6 Ma (Heiney Bar). During the interval between emplacement of these two satellite plutons, a regional thrusting and metamorphic event named the Siskiyou orogeny (Coleman et al., 1988) was responsible for tectonic imbrication of the lower crust (Allen and Barnes, 2006).

The central English Peak pluton (Fig. 1) is the largest component of the EPC, with an area of ca. 143 km^2. This pluton was emplaced in two stages (Schmidt, 1994). The early stage is heterogeneous at the outcrop scale and ranges from gabbro to tonalite, with U-Pb zircon ages from 160.4 to 156.6 Ma (Allen & Barnes, 2006; Ernst et al., 2016). The late stage, the focus of this paper, consists of quartz monzodiorite, tonalite, granodiorite, and granite. The late stage is zoned (Fig. 1), with inwardly-increasing proportions of quartz and K-feldspar, and decreasing color index (Seyfert, 1964). The late stage was subdivided on the basis of bulk-rock compositions (Schmidt, 1994; Barnes et al., 2016b) into the border unit, annular Yellow Jacket Ridge (YJR) unit, and interior Chimney Rock (CR) unit (Fig. 1). Contacts between units are gradational; however, blocks of the outer units are found in adjacent inner units, indicating an inward-younging emplacement sequence (Schmidt, 1994). U-Pb zircon ages of the late stage range from 156.3 ± 1.3 to 155.3 ± 1.2 Ma and are identical within analytical uncertainty (see Ernst et al., 2016, for detailed discussion of the geochronology). Contact metamorphism in the EPC aureole reached maximum temperatures of 500–600°C at 200–300 MPa (Hacker et al., 1992; Ernst, 1999) with local fluid exchange in the contact aureole (Ernst and Kolodny, 1997).

PETROGRAPHY OF LATE-STAGE SAMPLES

Most late-stage samples share similar textural and mineralogical features. With a few exceptions discussed below, the rocks are coarse-grained and hypidiomorphic granular, with broadly seriate grain-size distribution; Hbl and plagioclase grains reach 10 mm in length.

Border unit. Most samples from the northern border unit (e.g., EP-121, EP-126; Fig. 1) are Bi-Hbl tonalite. Plagioclase occurs as blocky, euhedral to subhedral tablets that are oscillatory-normal zoned ($An_{57–30}$; feldspar compositions determined by electron microprobe analysis, Schmidt, 1994; Barnes et al., 2016b), whereas quartz and K-feldspar are interstitial. Intergranular accessory minerals (apatite, ilmenite, and zircon) are sparse. Pleochroic dark-brown to medium-brown biotite is euhedral to subhedral, with minor inclusions of apatite, ilmenite, and zircon.

Yellow Jacket Ridge unit. Most samples are Bi-Hbl granodiorite, but tonalite, quartz monzodiorite, and rare granite are present. In general, YJR samples contain higher proportions of K-feldspar (~Or_{90}) and quartz (Barnes et al., 2016b); the K-feldspar tends to be poikilitic, enclosing euhedral Hbl, biotite, plagioclase, and quartz. Blocky plagioclase is oscillatory-normal zoned (An_{63-19}). Accessory minerals are apatite, zircon, and ilmenite.

Chimney Rock unit. Most CR samples are Hbl-Bi granodiorite or granite and some are porphyritic, with phenocrysts of Hbl, biotite, plagioclase, quartz, and locally K-feldspar. Medium- to dark-brown biotite is euhedral to subhedral and contains fine apatite inclusions. Plagioclase is generally blocky and oscillatory-normal zoned, typically from $An_{40–19}$, and sparse cores as calcic as An_{48}. In porphyritic samples, finely perthitic K-feldspar (~Or_{90}; Barnes et al., 2016b) appears to have formed as euhedral, Carlsbad-twinned tablets overgrown by interstice-filling K-feldspar. Inclusions in K-feldspar are plagioclase, quartz, Hbl, and biotite. In addition to accessory apatite, ilmenite, and zircon, CR samples are characterized by accessory allanite, which is rare or lacking in the other late-stage units. Intergranular titanite was observed in one CR sample.

Deuteric alteration is common throughout the late stage, but only rarely affects the entire volume of a sample. Saussuritization of plagioclase and K-feldspar is common, whereas alteration of biotite to chlorite ± white mica is less so. Alteration of amphibole is variable in intensity, both from sample to sample and within individual samples (see below).

Hornblende zoning and inclusion patterns.

Euhedral to subhedral Hbl is typically prismatic, although some hornblende ± biotite glomerocrysts are present. Individual Hbl grains exhibit olive-brown to tan pleochroic cores that are rimmed and embayed by medium-green, weakly pleochroic Hbl (Fig. 2A). The embayments are most pronounced in CR samples. It is noteworthy that olive-brown cores are present in all grain sizes. Alteration of Hbl is variable. In the least-altered samples, Hbl lacks alteration or displays minor replacement by biotite ± chlorite (Figs. 2A, B). Greater amounts of deuteric alteration result in partial to nearly complete replacement of the primary crystals by chlorite ± albitic plagioclase ± epidote ± actinolitic amphibole (e.g., Fig. 2C). This type of alteration is marked by primary grains riddled with deuteric minerals. However, in most samples remnants of both olive-brown cores and medium-green rims are preserved.

Hornblende contains inclusions of quartz, apatite, ilmenite, zircon, and, in some cases, biotite. Quartz inclusions occur as clusters of minute, anhedral grains near Hbl cores and are commonly surrounded by pale amphibole. These inclusions are products of reaction from pyroxene.

In contrast, inclusions of apatite, ilmenite, and zircon occur in the olive-brown cores, in the green rims, and in the transitions between cores and rims. Apatite is present as equant, euhedral to subhedral crystals and as short, needle-like grains typically oriented parallel to crystal faces (Fig. 2A). Ilmenite is typically present as minute, equant inclusions but also occurs as elongate, subhedral to anhedral grains as much as 100μm long (Fig. 2D). Zircon inclusions are much sparser than ilmenite and apatite and are generally sub-equant, although a few are elongate prisms (Figs. 2D, E). Biotite inclusions vary from equant crystals (Fig. 2A) to thin plates. Accessory allanite in the CR unit in contact with Hbl is only in contact with rims (Fig. 2B); it does not occur as an inclusion in Hbl.

Unusual samples. Tonalite RBEP-021 was collected <10 m from the northern intrusive contact of the northern border zone. This sample is texturally similar to nearby border zone samples. Orthopyroxene and relict pyroxene occur as cores in some Hbl grains. Hornblende is subhedral, displays medium- to pale-green pleochroism (Fig. 2F), and nearly lacks olive-brown zones, which occur as rare patches no more than 100 μm in diameter. Some Hbl clusters have interior zones of cummingtonite, presumably after orthopyroxene. Biotite in this sample is reddish brown.

Sample EP-267 was collected from an area referred to here as the southern border unit (Fig. 1; Schmidt, 1994; Barnes et al., 2016b). It is texturally similar to samples from the more extensive northern border and YJR units and contains cm-scale glomerocrysts of Hbl ± biotite.

Sample RBEP-024 from the northeastern tip of the CR unit is porphyritic Hbl-biotite granite with medium-grained granular groundmass. It contains phenocrysts of oscillatory-normal zoned plagioclase, subhedral quartz, and Hbl. The Hbl phenocrysts show typical color zoning and resorption, whereas groundmass Hbl and Hbl inclusions in plagioclase rims display the weakly pleochroic green color of phenocryst rims. In addition to Hbl, the groundmass consists of granular plagioclase, quartz, K-feldspar, and biotite. Accessory minerals are apatite, zircon, ilmenite, and metamict allanite.

METHODS

Hornblende and biotite major element concentrations were determined by electron microprobe (EMP) at the University of Oklahoma. Typical operating conditions were 20 kV accelerating voltage, 20 nA beam current, and ca. 1 μm spot size, using natural and synthetic standards. Hornblende and biotite contain negligible Cl and F (typically < 0.2 total wt%; Schmidt, 1994), therefore these elements were omitted in later analytical sessions. Hornblende cation site occupancies were estimated on the basis of 23 oxygens using the Esawi (2004) spreadsheet and were classified according to Leake et al. (1997). Trace element abundances were measured by in situ laser ablation-inductively coupled plasma-mass spectrometry (LA-ICP-MS) on polished sections using a NewWave 213 nm solid-state laser and Agilent 7500CS ICP-MS at Texas Tech University. Nominal operating conditions were spot diameter 40 μm and laser pulse rate of 5 Hz. During the study, a dual-volume sample cell was installed. Analyses carried out in the older, single-volume cell used a fluence of 11–12 J/cm^2, whereas analyses carried out in the dual-volume cell used a fluence of ca. 6 J/cm^2. For each analysis, 25s of background (laser off) and 60s of signal were recorded. The primary analytical standard, NIST 612 glass, was analyzed after every 5–10 unknowns. Precision was determined by repeated analysis of basaltic glass BHVO-2g. Long-term precision (RSD) ranges from 2.5–12% and is < 7% for most trace elements; after installation of the dual-volume cell, precision improved to 2.1–9.2%, and <6% for most trace elements). Accuracy as measured compared to basaltic glass BHVO-2G was better than 5% relative for Sc, Mn, Ni, Cu, Zn, Rb, Ce, Pr, and Ta and 10% for V, S, Nb, Ba, La, Nd, Sm, and Eu. Analyses of Gd, Dy, Er, Tm, and Yb were routinely 15% low and those of Y, Zr, Tb, Ho, Tm, Lu, and Hf were routinely 20% low. The poor accuracy of the latter two groups of elements was traced to use of the NIST 612 glass standard. Our lab currently uses U.S. Geological Survey glass standard GCD-G, which has improved accuracy of all analyzed elements in BHVO-2G to better than 10% relative. This change was made after the analyses reported here, so no intra-lab adjustment was necessary. Trace element abundances were normalized to that of CaO for amphibole and SiO_2 for biotite, as determined by electron microprobe. Wherever possible, LA spots were located on or adjacent to EMP analytical spots. Comparison of MnO and Al_2O_3 concentrations determined by EMP and LA-ICP-MS shows good correlation. Nevertheless, differences in analytical volumes between the two methods dictate that such correlations cannot be perfect. All LA spectra and reduced data were inspected for anomalously high counts and/or spikes of P, Ti, and Zr to avoid analysis of small inclusions; these anomalous analyses were omitted from the data set. Limits of detection of elements reported here are nearly all less than 1% of the abundance reported, but reach 5% for Rb and Ta and 13% for Th and U. Trace element contents of allanite were determined by LA-ICP-MS using ca. 6 J/cm^2 fluence, 20 μm spot diameter, and laser pulse rate of 5 Hz. Calibration was to NIST 610 glass, using stoichiometric CaO contents for internal standardization.

RESULTS

In addition to the new data reported here, we have utilized EMP data presented in earlier studies (Schmidt, 1994; Berry, 2015; Barnes et al., 2016b). Some of our new analyses were made on previously-analyzed samples, and in all cases inter-laboratory variability is negligible.

Amphibole compositions

Major and minor element analyses define a near-continuum of compositions from tschermakitic cores through intermediate zones of magnesiohornblende to local actinolitic rims (Supplementary Data 1). Olive-brown cores are tschermakite–magnesiohornblende, with tschermakite typical of the interiors of core zones (Fig. 3A). The green rims and embayed zones are magnesiohornblende. Pale green to colorless deuteric amphibole is generally rich enough in Si to be classified as actinolite. Amphibole compositions classified as tschermakite typically have lower Si and slightly higher Mg# [Mg/(Mg+Fe$_{total}$)] than those classified as magnesiohornblende (Fig. 3A). In addition, and despite the scatter in Mg#, the olive-brown cores can be distinguished from green rims on the basis of Si: core zones have < 7 Si atoms per formula unit (apfu), whereas green rims and embayed zones have Si from 7.0–7.5 apfu. Hbl from the porphyritic sample of the CR unit (RBEP-024) has distinctly lower Mg# (Fig. 3A). However, as with other Hbl, the boundary between olive-brown cores and green rims in this sample is at ca. 7.0 Si apfu.

The abundance of Na decreases monotonically with increasing Si (Fig. 3B). In addition, at a given Si value, Hbl from the northern border unit has the lowest Na and Hbl from the CR unit has the highest. It is noteworthy that Na in Hbl from the southern border unit (sample EP-267) overlaps with compositions of YJR Hbl rather than with Hbl from the northern border unit. Titanium abundances also decrease with increasing Si. However, an apparent change in slope in the Si–Ti diagram occurs at a Ti value of ca. 0.15 apfu (Fig. 3C), which corresponds to an Si value of 7.0: the boundary between cores and rims. In contrast, Mn contents increase with increasing Si (Fig. 3D). No distinction exists between border and YJR units in terms of Mn; however, samples from the CR unit have higher Mn contents, with the highest values in porphyritic sample RBEP-024.

The abundance of Zr is well correlated with that of Ti (Fig. 4A). Within individual samples, Zr decreases with decreasing Ti, with the transition from olive cores to green rims occurring at 55–60 ppm Zr. The abundances of Sr, Eu, and Hf decrease monotonically with decreasing Zr (Fig. 4B, C, D), with each element showing an ~5-fold decrease from cores to rims. The abundance of Ba decreases from as much as 400 ppm to ca. 1 ppm in an S-shaped pattern (Fig. 4E): Ba is approximately constant at ca. 350 ppm in interiors of core zones, decreases to 100–

140 ppm at core–rim boundaries, then decreases toward detection limits in the rims. Rubidium and Cr contents (not shown) follow a similar pattern but with more scatter.

In contrast to the simple monotonic zoning patterns described above, variation of Sc, Y, and the middle and heavy rare earth elements (REE) are more complicated (Fig. 4F–J). The abundances of these elements decrease in the olive cores to a minimum value and then either remain constant, as in the border unit, or increase, as in the YJR and CR units. In the border unit, the minimum concentrations coincide with the boundary between olive-brown cores and green rims. However, in the YJR and CR Hbl, the minimum concentrations occur within the olive-brown core zones at Zr concentrations of ca. 80–85 ppm, which corresponds to Ti contents of 11,000–14,000 ppm (1.8–2.3 wt% TiO_2). With further decrease in Zr contents in the YJR and CR amphiboles, Sc, Y, and the middle and heavy REE increase abruptly. The magnitude of the increase varies from sample to sample and element to element, but reaches as much as 100% for Sc in YJR samples and as much as 400% is some CR samples (e.g., Y; Fig. 4G).

The variation of Nb (Fig. 4J) and Ta (not shown) is negligible in core zones. However, at the core–rim boundary, both Nb and Ta abundances decrease. Then, in some analyses from green rims and embayed zones, both Nb and Ta abundances display an abrupt increase.

Rare earth element patterns also vary systematically from core to rim and as a function of Zr content. With decreasing Zr contents in olive-brown cores, the size of the negative Eu anomaly (Eu/Eu*) decreases (Fig. 4K) and the slope of the REE pattern increases (Fig. 4L). However, with the exception of a single sample noted below, as Zr decreases in the green rims and embayed zones, the slope of the REE pattern (La_N/Lu_N) decreases. In contrast, the depth of the europium anomaly increases in rims of Hbl from the YJR and CR units, but not in the border unit (Fig. 4K). These changes in the shape of the REE patterns are also illustrated in Figure 5, in which representative data are plotted in order to avoid obscuring individual zoning relationships. The olive-brown core zones typically display a convex pattern in the light REE, and the convexity increases in green rims and embayed zones. The tendency for increasing abundances of heavy REE in the rims of some YJR and most CR samples can be seen in Figure 5B–D and is most pronounced in the late-stage CR sample RBEP-024 (Fig. 5E). This increase in heavy REE combined with the deepening Eu anomaly lead to a gull-wing-like pattern (e.g., Fig. 5D, E).

Unusual samples. The border unit sample collected near the northern contact (RBEP-021) is distinct in that nearly all Hbl exhibits weak medium-green to pale green pleochroism; however, a few grains contain small patches of olive-brown Hbl. These olive-brown patches have Si from 6.8–7.0 (apfu), whereas the remainder of the Hbl has higher Si contents (Fig. 3). In addition, with the exception of the REE, the olive-brown patches have trace element abundances similar to the outer cores of other border unit samples. The remaining analyzes from this sample display lower abundances of Sc, Nb, Y, and the REE (Fig. 4) and higher abundances of Mn (Fig. 3D) than is seen in other border zone samples. All REE patterns, whether from olive-green or green Hbl, display a 'reverse-J' shape, unlike the convex patterns of Hbl from other border zone samples (Fig. 5A).

In sample EP-267 from the southern border unit, olive-brown Hbl core compositions are similar to those of Hbl from YJR rocks. In particular, the Hbl has higher Mg#, Na, and La/Lu and lower Ti, Sc, Ba, and REE than does Hbl from the northern border unit. These data suggest that the southern and northern border units are not correlative.

Biotite and allanite compositions. In order to better understand trace element zoning in amphibole, major and trace element compositions of biotite and trace element compositions of allanite were measured (Supplementary Data 2). Major element data on biotite were presented by

Barnes et al. (2016b). Biotite shows little variation throughout the late stage; for example, Mg# varies from 0.48 to 0.52 in all analyzed samples. Biotite from two samples was analyzed on a reconnaissance basis for trace element abundances. Compared to Hbl, abundances of V, Cr, Rb, Nb, Ta, and Ba in biotite are relatively high, whereas abundances of Sr, Y, Zr, Hf, and the REE are low to very low.

Trace element abundances in allanite from CR sample RBEP-022 are typical of igneous allanite, with high Y, light REE, Th, and U contents. The REE patterns of these allanite grains have steep negative slopes, with a decrease in slope from Tm to Lu and a prominent negative Eu anomaly (Fig. 5F).

THERMOBAROMETRY

Estimates of the conditions of magma storage and final emplacement were presented by Barnes et al. (2016b, their Fig. 13) on the basis of a pseudosection calculated for a YJR granodiorite and on a range of thermobarometric calculations (Schmidt, 1992; Anderson and Smith, 1995; Ernst & Liu, 1998; Putirka, 2016). The pseudosection calculations indicated Hbl stability at T > 850°C, biotite crystallization at T ca. 810°C, at or below the depth of emplacement, and quartz crystallization at T ≤ 750°C.

Temperature was calculated using Putirka's (2016) pressure-independent equation 5, which reproduces calibration data to ± 30°C. The thermometer is based on major element concentrations, so that calculated temperatures can be directly compared to electron microprobe data. For example, calculated T is well correlated with Ti (Fig. 6). The thermometric results indicate Hbl crystallization temperatures decreased monotonically from as high as 880°C in cores to as low as 690°C in rims, with actinolite T from ca. 660–690°C. The boundary between cores and rims is at ~760°C (Fig. 6), but in detail, the majority of core temperatures cluster above about 780°C, whereas the majority of rim temperatures cluster below about 750°C. The computed solidus at 200–300 MPa is ca. 700°C (Barnes et al., 2016b), which indicates that the green rims and embayed zones are magmatic, whereas actinolite (s.s.) is a subsolidus phase. This conclusion agrees with work by Pe-Piper (1988), who concluded that the transition from magmatic to sub-magmatic Hbl in granodioritic rocks from Nova Scotia was at Ti contents of ca. 0.05 apfu.

Pressure estimates using the Al-in-hornblende geobarometer (Schmidt, 1992) were interpreted by Barnes et al. (2016b) to indicate that olive-brown Hbl cores crystallized at ca. 420 MPa, whereas the medium-green rims crystallized at ca. 220 MPa. The latter pressure is consistent with an emplacement pressure of 200–300 MPa, made using contact metamorphic assemblages (Hacker et al., 1992; Ernst, 1999). Further consideration of Hbl barometry indicates that the Hbl rims crystallized at temperatures low enough, and in equilibrium with minerals appropriate for, application of traditional Al-in-hornblende geobarometry (Hammarstrom and Zen, 1986; Hollister et al., 1987). However, it is unlikely that Hbl cores crystallized in equilibrium with quartz, and it is unclear if Hbl crystallization temperatures were appropriate for use of traditional Al-in-hornblende barometry (cf. Anderson and Smith, 1995). Moreover, there is no correlation between calculated site occupancies of ^{IV}Al and ^{VI}Al, as would be expected from pressure-sensitive Al-Tschermaks exchange. In contrast, ^{IV}Al is well correlated with Ti and ^{A}(Na+K), which indicates that the bulk of variability in Hbl is related to temperature-sensitive Ti-Tschermaks and edenite exchanges (cf. Helz, 1982; Hammarstrom and Zen, 1986; Anderson and Smith, 1995).

In an attempt to refine and clarify conditions of core crystallization, we applied the approach of Anderson and Smith (1995), which combines the Al-in-hornblende geobarometer with amphibole-plagioclase exchange thermometers (Blundy and Holland, 1990; Holland and Blundy, 1994). Results of these calculations using An_{35} plagioclase in equilibrium with Hbl cores and An_{30} in equilibrium with Hbl rims yielded P estimates of ca. 280 MPa (cores) and 210 MPa (rims), leaving in question the magnitude of pressure change between core and rim crystallization.

DISCUSSION

Magmatic units in the late stage of the English Peak pluton

Gradational contacts between late-stage units led Seyfert (1964) to interpret the late stage as forming from a single, differentiating magma. In a general sense, the chemical continuum of Hbl compositions supports this concept, although the distinctly lower Na in border unit Hbl and higher Mn in CR unit Hbl (Fig. 3) indicate a more complicated magmatic history. On the basis of Schmidt's work (1994), Barnes et al. (2016) proposed an alternative emplacement history, in which variations in late-stage bulk-rock compositions reflect three distinct magma pulses. These interpretations may now be tested on the basis of Hbl compositions.

Hornblende cores from the northern border unit have distinctly higher abundances of Ti, Ba, and Sc, and lower Na than Hbl cores from the YJR and CR units (Figs. 3 and 4). On this basis, we suggest that magmas parental to the northern border unit were distinct from, albeit similar to, magmas parental to the interior YJR and CR units. In contrast, Hbl cores in the sample from the southern border unit show similarities with Hbl cores in the adjacent YJR unit, rather than the northern border unit. Thus, although additional data are needed, it appears that the northern and southern border units are not comagmatic. Instead the southern border unit could: (1) be a distinct magmatic unit with parental magma(s) similar to those of the YJR; (2) represent cumulates from YJR magmas and therefore part of the YJR; or (3) represent a hybrid between exterior early-stage and interior YJR magmas.

Most major and trace element contents of Hbl cores from YJR and CR samples are similar and display nearly total overlap (Figs. 3 and 4). Nevertheless, the cores of CR Hbl are distinct in having slightly higher Na (Fig. 3B) and significantly higher Mn contents (Fig. 3D). It therefore appears that magmas parental to the YJR unit were distinct from those parental to the CR unit.

In summary, the Hbl data indicate that although similar, the northern border, YJR, and CR units display small but measurable compositional differences. We infer from the similarities that a mid-crustal magma reservoir in which EPC magmas were stored gave rise to successively evolved magma batches. These differences in Hbl compositions imply that Hbl cores in YJR and CR samples are not antecrystic (inherited) from the older border unit magmas. Instead, they indicate that evolution within the mid-crustal magma chamber(s) resulted in subtle, successive changes in magma compositions prior to final, pulsed emplacement into the upper crust.

Magma evolution

If the chemical zoning in magmatic Hbl records changes in melt composition, then the data provide information about nearly 200°C of magma evolution, a significant part of the magma's history. A summary of the types of trace element zoning is shown graphically in Figure 7.

The approximately linear decreases in many minor and trace element abundances (e.g., Ti, Zr, Sr, Ba, Eu, Hf) from the interiors to the edges of olive-brown Hbl cores can potentially be explained by fractional crystallization, magma mixing, and diffusional exchange between Hbl crystals and surrounding melt. The process of diffusional control of trace element variation is difficult to support, because elements such as Ti and Zr would be expected to diffuse extremely slowly compared to Sr and Na, yet these elements share similar zoning patterns. In addition, although we are not aware of published diffusion coefficient data for Ti in calcic amphiboles, at the temperatures discussed here for the EPC system (<900°C), Ti diffusion in diopside and Cr-diopside has ceased (Cherniak and Liang, 2012). It seems likely that the same conclusion may be reached for HFSE (and REE) in Hbl. Moreover, late-stage exchange of trace elements by diffusion and/or annealing should result in homogenous abundances in individual grains, with regard to both major and trace element concentrations. However, as seen in Figure 2G, boundaries between cores and embayed zones are sharp. One possible exception is sample, RBEP-021 from the northern border unit (Figs. 3, 4), in which the nearly uniform green color of Hbl could be the result of homogenization due to diffusion. However, an alternative explanation is presented below.

The presence of mafic magmatic enclaves and synplutonic mafic dikes is permissive evidence for magma mixing in late-stage magmas (Schmidt, 1994). However, if the compositions of the mafic magmatic enclaves and synplutonic mafic dikes (Barnes et al., 2016b) are representative of the mafic input, then magma mixing should have resulted in distinct reversals in zoning patterns of elements like Ti, the contents of which are higher in mafic enclaves and dikes than in late-stage rocks (Barnes et al., 2016b). Such reversals are absent. Mixing with evolved (rhyolitic) magmas should result in abrupt, step-like decreases in Ti and in compatible trace elements such as Sr and Ba; this type of decrease was also not observed.

Trace element variation in Hbl could also be due to crystal chemical controls, and particularly to the effects of coupled substitutions. For example, the decrease in 3^+ and 4^+ trace elements from the interiors to the exteriors of olive-brown cores (e.g., Zr, Hf, Y, Sc, REE) correlates with decreasing Ti and Al. However, the decrease in many 3^+ cation abundances ceases at about 80 ppm Zr, *within* the olive brown cores, even though Ti and Al continue to decrease. This change of slope in the element trends suggests that the primary controls on trace element zoning were changing melt composition and bulk partition coefficients, rather than changes in the nature of coupled substitutions. Changes in mineral/melt and bulk partition coefficients are, in turn, functions of T, melt composition, Hbl composition, and the fractionating phase assemblage (Shimizu et al., in press). The following section explores the effects of fractional crystallization on observed major and trace element variations in Hbl.

If the decrease in trace element abundances from interior to margins of the olive-brown Hbl cores is due to fractional crystallization, then it is possible to construct models for this variation. The simplest case is one in which mineral/melt and bulk partition coefficients are essentially constant over a range of temperatures. In this case, the Rayleigh equation can be recast in terms of mineral compositions. This approach to modeling was used by Barnes et al. (2016c) and is explained in detail with a summary of pertinent mineral/melt partition coefficients in Supplementary Data 3. An example, is variation of Zr and Sr in Hbl, whose abundances decrease continuously from interiors of olive-brown cores to embayed zones and green rims (Fig. 8A). Because Sr is incompatible in Hbl and Zr varies from incompatible to weakly compatible at low T (Tiepolo et al., 2007; Nandedkar et al., 2016), the core-to-rim decreases in these two elements mean that both were compatible in the system; that is, both had *bulk* partition coefficents >1. Therefore, the linear decreases may be modeled in terms of simple fractional crystallization. Such models are non-unique because as long as the ratio of the two bulk partition coefficients is constant, models will show linear decrease. This situation is illustrated in Figure 8A, in which the model shown with black squares ($D_{Zr} = 3.0$, $D_{Sr} = 3.2$) is collinear with the model shown with gray squares ($D_{Zr} = 2.0$ and $D_{Sr} = 2.1$). The difference between these two models, and any similar models, is the proportion of melt remaining (F), as shown by the tic marks on the model curves. Nevertheless, there are logical limits to D values. For example, a model with $D_{Zr} = 1.5$ and $D_{Sr} = 1.6$ fits the data, but the calculations indicate that the magma would be 80% solidified at the time green rims began to crystallize. Such a magma would be immobile, yet the P-T data indicate that the core-to-rim transition was related to magma migration from a deeper reservoir. Therefore, we assign an initial D_{Zr} value of ca. 3.0 in the following discussion; this value leads to an estimated value of F at the core–rim boundary of ca. 0.7.

It is axiomatic that D values for most trace elements vary as F decreases. This variation is due to changes in the fractionating assemblage and to the fact that for many trace elements individual mineral/melt partition coefficients increase with decreasing T, increasing melt polymerization, and changing melt composition (e.g., Zhang et al., 2017). Figure 8B presents a fractional crystallization model in which D_{Zr} is constant but D_{Ba} increases linearly from a value of 1.0 at $F = 0$ to a value of 9.0 as F approaches zero. This model fits the nearly constant values of Ba in the interiors of olive-brown cores, followed by the abrupt decrease in Ba in core zones. Such an increase in D_{Ba} is readily explained by appearance of biotite as a fractionating phase during crystallization of olive-brown Hbl (Fig. 7; Supplementary Data 3).

The variation of many of the 3^+ trace elements, which decrease in olive-brown cores, then remain essentially constant, and then increase in abundance at still lower Zr contents (Fig. 4F–I), cannot be modeled by simple fractional crystallization. The essentially constant values of these elements in the Zr concentration range of 80–50 ppm suggests that bulk partition coefficients for the 3^+ elements decreased abruptly as T decreased (see further discussion in Supplementary Data 3). Moreover, if the increase in these elements in the outer parts of crystals was due to fractional crystallization, the implication would be that the 3^+ trace elements were nearly perfectly incompatible at temperatures close to the solidus: an unlikely situation. For the sake of illustration, this dramatic decrease in D is modeled in Figure 8C, in which D_Y decreases from 5.0–0.1 and D_{Zr} decreases from 3.0–2.0. Although the model curve fits much of the data, it is difficult to imagine such low D_Y values in a magmatic environment in which Hbl, apatite, and zircon were crystallizing (also see below and Supplementary Data 3).

An alternative approach to modeling variation of the 3^+ trace elements is shown in Figures 8D and E. In these examples, the initial collinear decreases in Sc and Sm with Zr are modeled by fractional crystallization in which all three elements are compatible. However, at an F value of 0.8 (black dashed curve), Sc and Sm become slightly incompatible (D = 0.9) and D_{Zr} increases to 5.0. The resulting model fits trace element variation in the range of Zr contents from 80–50 ppm.

What can explain this decrease in D for the nominally compatible elements Sc and Sm? In the YJR and CR Hbl, the change from compatible to slightly incompatible behavior occurs within the olive-brown cores at Zr contents of ca. 80 ppm, in the T and compositional range inferred for the appearance of biotite on the liquidus (Fig. 8). The abundances of both Sc and Sm are low in biotite (<15 ppm Sc; < 2 ppm Sm; Supplementary Data 2). Thus, coprecipitation of biotite and Hbl will have the effect of lowering D for elements like Sc, the REE, and Y. Therefore, even if the Hbl/melt partition coefficient increased, we infer that D decreased to approximately 1.0 when biotite began to crystallize.

If decreasing D can explain the near-constant values of the 3^+ elements in Hbl interiors, then it is logical to ask whether a further decrease in D to very low values can explain the abrupt increases in 3^+ trace elements, plus Nb and Ta, in the green rims and embayed zones (i.e., < 50 ppm Zr). We infer that such increases in element abundances are impossible by fractional crystallization in a closed system, because under the conditions at which the rims and embayed zones became stable, the abundances of these trace elements in the rhyolitic melt phase would have been negligible (see Supplementary Data 3 for more detail). The lack of titanite in these rocks means that in late-stage EPC magmas, the 3^+ cations were sequestered primarily in Hbl, whereas Nb and Ta are sequestered in both biotite and Hbl.

A second possibility is that the enrichment in the 3^+ cations, Nb, and Ta was due to magma mixing. However, as discussed above, there are no major element zoning reversals in Hbl or plagioclase (Schmidt, 1994) that would provide support for late-stage mixing. A third possibility is that the rim-ward enrichment is the result of deuteric alteration. We view this process as unlikely because the T estimates for green Hbl rims indicate crystallization from a melt (Fig. 6).

The similarity in compositions of green rims and embayed zones suggests that crystallization of green Hbl either followed, or was accompanied by, resorption of olive-brown cores. We ascribe this resorption event to changing P-T conditions associated with rise of the magmas from a deeper reservoir to the level of emplacement. This conclusion is supported by the fact that a temperature gap exists between olive-brown cores and green rims (see above). When Hbl stability was re-established, green Hbl crystallized. Resorption would release cations sequestered in olive-brown Hbl to the melt. These elements would then be incorporated in the stable phases: Sr into plagioclase, Ba into biotite ± K-feldspar, Zr and Hf into zircon, the 3^+ cations into the newly-crystallized green Hbl, and Nb and Ta into biotite and green Hbl. In the case of the late-stage magmas, 3^+ cations were most likely to be incorporated into green Hbl, because of the absence of titanite and because apatite crystallization was limited owing to prior sequestration of P_2O_5 into apatite at higher T.

An equation describing resorption followed by crystallization was derived by Shaw (2006). The equation and input parameters are given in Supplementary Data 3 and results are illustrated in Figures 8D and E. In these illustrations, resorption begins at a Zr content in Hbl of ca. 55 ppm, which corresponds to the core–rim boundary and to a nominal fraction of melt remaining of 0.7. The resulting models coincide with the zoning patterns in Hbl from the CR unit, which shows the greatest amount of enrichment of 3^+ cations. The smaller enrichments characteristic of the YJR and border units can be readily modeled by decreasing the mass ratio of resorbed core/crystallized rims (see Supplementary Data 3).

In summary, the lack of compositional reversals suggests that trace element zoning was unrelated to magma mixing at the emplacement level. Instead, we suggest that: (1) decreasing Sr and Zr indicate that plagioclase and zircon co-precipitated with olive-brown cores; (2) decreasing Ti resulted from fractionation of hornblende and ilmenite, and ultimately biotite; (3) biotite crystallization began during crystallization of Hbl cores, as indicated by changes in Ba, Rb, and Cr from essentially incompatible to compatible (Fig. 8); (4) biotite crystallization also resulted in previously compatible elements (Sc, Y, REE) becoming either weakly compatible or weakly incompatible; and (5) changing P-T conditions accompanying final magma emplacement resulted in resorption of olive-brown Hbl, followed by crystallization of green Hbl that infilled resorbed zones and rimmed the cores. The effects of resorption are most pronounced in the interior, most evolved Chimney Rock unit, which suggests that these magmas had the largest proportion of residual melt.

Calculated melt compositions

The trace element data permit estimation of melt compositions in equilibrium with Hbl if appropriate Hbl/melt partition coefficients are available. These estimates must be made with caution because of the relationship between partition coefficients and T. For example, estimated melt Zr contents were calculated using two $d_{\mathrm{Hbl/melt}}$ values: 0.68 (Klein et al., 1997) and 1.0

(Nandedkar et al., 2016). Use of the lower $d_{Hbl/melt}$ value yields Zr contents in melts in equilibrium with olive-brown cores as high as 210 ppm andca. 75 ppm at core–rim boundaries. The range of calculated melt Zr contents in equilibrium with olive-brown cores compares well with bulk-rock Zr contents (Fig. 9; Barnes et al., 2016b). In contrast, if $d_{Hbl/melt} = 1.0$, the range of Zr contents of melts in equilibrium with olive-brown cores is ca. 135–40 ppm and bulk-rock Zr contents are higher than calculated melt compositions. In this latter case, one must conclude that the higher Zr contents in the bulk rocks must be due to zircon accumulation.

Calculation of REE abundances of melts in equilibrium with Hbl results in similar uncertainties. Calculated REE patterns for five EPC samples (Fig. 10) illustrate the effects of the choice of $d_{Hbl/melt}$ values. In panels A, C, D, and E, the olive patterns represent melts calculated to be in equilibrium with Hbl cores using $d_{Hbl/melt}$ values from Klein et al. (1997) and the blue patterns represent the same calculations using Nandedkar et al. (2016) $d_{Hbl/melt}$ values. For simplicity's sake, only the Klein et al. (1997) $d_{Hbl/melt}$ values were used to calculate melt REE patterns in equilibrium with Hbl rims. In each panel, bulk-rock REE patterns are also plotted.

Neither set of melt compositions calculated from olive-brown core data precisely matches the bulk-rock REE abundances, but both sets approximate the *shapes* of the bulk-rock REE patterns. The two sets of $d_{Hbl/melt}$ values are distinct in that calculated melts based on the Klein et al. (1997) data either lack Eu anomalies or display small negative anomalies, whereas the Nandedkar (2016) values result in prominent negative anomalies in all calculated melts. Calculated melt REE patterns for sample RBEP-024 from the Chimney Rock unit are distinct because all calculated melt compositions are higher than the bulk-rock composition. This sample also displays a distinct relationships between Hbl cores and rims: melts calculated from green

This is a preprint, the final version is subject to change, of the American Mineralogist (MSA)
Cite as Authors (Year) Title. American Mineralogist, in press.
(DOI will not work until issue is live.) DOI: http://dx.doi.org/10.2138/am-2017-6063

rim compositions display REE patterns with shallow slopes, deep negative Eu anomalies, and higher heavy REE than melt calculated from core compositions (Fig. 10E).

Calculated melt REE patterns for northern border unit sample RBEP-021 have reverse-J shapes that are distinct from the other samples but reproduce the bulk-rock REE pattern (Fig. 10B). Barnes et al. (2016b) interpreted the shape of the bulk-rock REE pattern to be the result of accumulation of feldspars, on the basis of the positive Eu anomaly and low heavy REE abundances. However, the similarity of the calculated melt REE pattern and the bulk-rock pattern suggests that the bulk-rock pattern owes its origin to the composition of melt, whether or not the rock is a cumulate. The reverse-J shape is generally interpreted to indicate relatively extensive Hbl and/or titanite fractionation (e.g., Marks et al., 2008; Glazner et al., 2008; Davidson et al., 2013). If correct, then the magma from which sample RBEP-021 crystallized had undergone significantly more Hbl ± titanite fractionation than is seen in any other part of the late-stage EPC. Such differences are not evident in the field because sample RBEP-021 is megascopically similar to other border-zone samples. As noted above, Hbl in this sample is green, nearly lacking olive-brown patches, and titanite is absent. Therefore, we interpret this sample to have crystallized from a magma heavily fractionated by Hbl prior to final emplacement. It is unclear whether fractionation occurred in the deeper magma reservoir, or at the upper crustal level of emplacement.

Zoning in “ugly” hornblende

One of the goals of this work was to address a question common to the study of most minerals from plutonic rocks: how well do minerals such as Hbl preserve records of changing T and melt composition? A number of recent studies utilized trace element distribution and zoning patterns in attempts to reconstruct magma evolution (e.g., Claeson et al., 2007; Turner et al.,

Always consult and cite the final, published document. See http:/www.minsocam.org or GeoscienceWorld

2013; Coint et al., 2013; Leuthold et al., 2014; Otamendi et al., 2016; Barnes et al., 2016c). However, the fact that calcic amphibole is stable above and below the solidus means that care must be taken in assessing the conditions of crystallization prior to interpretation of the causes of trace element variation. In addition, Challener and Glazner (2017) described Hbl from the Half Dome Granodiorite riddled with inclusions and partly altered to minerals we consider to result from deuteric alteration. Challener and Glazner (2017) concluded that such Hbl crystals were unsuitable for geobarometric calculations. Setting aside the fact that Hbl geobarometry is problematic (Putirka, 2016), our results suggest that with appropriate methodology, plutonic Hbl is well suited as an indicator of magma evolution.

Our workflow (also Coint et al., 2013; Barnes et al., 2016c) begins with initial petrographic characterization and analysis of Hbl lacking appreciable alteration and with crystal habits, color zoning, and inclusions parallel to crystal faces (e.g., Fig. 2A); all of which indicate magmatic growth. Knowledge gained from analysis of these essentially unaltered crystals was then used to choose analytical spots in grains with abundant magmatic inclusions (plagioclase, biotite, apatite, and ilmenite) as well as significant deuteric alteration to chlorite ± actinolite ± epidote. Detailed petrographic examination followed by EMP analysis and then by T calculations showed that even in crystals with moderate deuteric alteration, magmatic Hbl can be identified and analyzed. In most cases, zoning patterns in individual crystals could be determined, thereby providing targets for LA trace element analysis. The example of border zone sample RBEP-021 was particularly instructive. We initially considered Hbl in this sample to be the result of late-stage exchange. However, T estimates and calculated melt compositions (Fig. 8B) indicate that the Hbl crystallized from a highly evolved magma and does not reflect subsolidus equilibration.

Support for our conclusions concerning the use of Hbl zoning patterns includes (1) calculated T of cores and most rims are higher than the computed solidus for a typical EPC granodiorite; however, calculated T for grains or zones identified as actinolite are typically subsolidus values; (2) we observed a striking change in the behavior of Ba, Cr, and Rb zoning in Hbl that is readily associated with the onset of biotite crystallization; (3) comparison of EPC Hbl with Hbl from volcanic systems demonstrates strong compositional and T similarities, particularly with the Okataina rhyolites from the Taupo center (Fig. 3B–D; Deering et al., 2011; Shane and Smith, 2013). In this comparison, it is noteworthy that the range of volcanic amphiboles encompasses both core and rim compositions of EPC Hbl, suggesting that the green rims are not subsolidus phases. It is also interesting to note that the lowest Ti in the volcanic Hbl is ca. 0.08 Ti apfu, whereas a few of the plutonic Hbl compositions have lower Ti (Fig. 3C). This Ti value is slightly higher than the 0.05 Ti apfu considered by Pe-Piper (1988) as the transition from magmatic to sub-solidus Hbl.

SUMMARY AND IMPLICATIONS

Magmas that formed the late stage of the EPC began crystallization at temperatures ≥ 880°C in one or more reservoirs below the level of emplacement. Decreasing Zr in Hbl cores indicates that Hbl and zircon co-precipitated from the beginning of Hbl crystallization. Inflections in Ba and Rb zoning patterns mark the appearance of biotite at ca. 810°C. We interpret the gap between calculated core and rim temperatures (ca. 780°C to 750°C) to mark ascent of the magmas to an upper crustal emplacement level. The change in T–P conditions was accompanied or followed by resorption of early-formed olive-brown Hbl, followed by resumed crystallization of green Hbl that infilled resorbed zones and rimmed the cores. Thus, as the magma rose to emplacement level, it carried a crystal cargo of plagioclase, Hbl, biotite, zircon, apatite, and ilmenite. Nevertheless, no evidence of antecrystic Hbl was found. This lack of antecrystic Hbl is consistent with the absence of antecrystic zircon in the pluton (Ernst et al., 2016).

This study illustrates the use of combined EMP and LA-ICP-MS analyses of Hbl from calc-alkaline plutonic rocks to provide multiple avenues to assess petrologic processes and changes in melt composition, and to relate these phenomena to temperature. The ability to calculate Hbl crystallization temperatures on the basis of major element contents, independent of melt composition, permits trace element zoning to be correlated with T, at least in a relative sense. Thus, intra-crystalline zoning of major and trace elements can be used to indicate phases that co-precipitated with Hbl and the thermal range over which these phases crystallized. For example, our results indicate that in the late-stage EPC magmas, zircon crystallization began at much higher T (ca. 880°C) than is indicated by zircon saturation thermometry (<770°C).

In this and other recent studies of trace element zoning in plutonic Hbl (e.g., Coint et al., 2013; Barnes et al., 2016c), most trace elements behave compatibly in the crystallizing magma. By choosing appropriate D and $d_{\mathrm{Hbl/melt}}$ values, despite the inherent uncertainties, intracrystalline zoning may be modeled in terms of fractional crystallization, resorption, and potentially in terms of magma mixing.

Finally, it appears that resorption of Hbl resulted in release of 3^+ cations, Nb, and Ta to the melt. Because this resorption occurred in the absence of sphene, these elements were temporarily enriched in the melt. If this interstitial melt had been separated from the crystal mush, its REE pattern would have had a gull-wing shape (e.g., Fig. 10E), unlike REE patterns considered to be characteristic of high-silica arc magmas.

ACKNOWLEDGEMENTS

This study utilized mapping, sampling, and petrographic descriptions in Ph.D. dissertations by Seyfert (1964) and Schmidt (1994) and our field work was assisted by Ken Johnson, Katie Gates, and David Atwood. We thank Kevin Werts and George Morgan for their able assistance in the laboratory and John Dilles for interesting discussions about plutonic hornblende. The manuscript was improved by helpful reviews by Madeleine Humphreys and Jade Star Lackey and editorial handling by Adam Kent. Early stages of this work were supported by NSF grants EAR-8720141 and EAR-9117103 to Barnes

REFERENCES CITED

Allen, C. M. and Barnes, C. G. (2006) Ages and some cryptic sources of Mesozoic plutonic rocks in the Klamath Mountains, California. In Snoke, A. W. and Barnes, C. G. (eds.) Geological studies in the Klamath Mountains province, California and Oregon: A volume in honor of William P. Irwin. Geological Society of America Special Paper, 410, 223–245.

Anders, E. and Grevesse, N. (1989) Abundances of the elements: Meteoritic and solar. Geochimica et Cosmochimica Acta, 53, 197–214.

Anderson, J. L. and Smith, D. R. (1995) The effects of temperature and fO_2 on the Al-in-hornblende barometer. American Mineralogist, 80, 549–559.

Bachmann, O., and Bergantz, G.W. (2004) On the origin of crystal-poor rhyolites: Extracted from batholithic crystal mushes. Journal of Petrology, 45, 1565–1582.

Bachmann, O., and Dungan, M. (2002) Temperature-induced Al-zoning in hornblendes of the Fish Canyon magma, Colorado. American Mineralogist, 87, 1062-1076.

Bachmann, O., Dungan, M. A. and Bussy, F. (2005) Insights into shallow magmatic processes in large silicic magma bodies: the trace element record in the Fish Canyon magma body, Colorado. Contributions to Mineralogy and Petrology, 149, 338–349.

Bacon, C. R., Newman, S. and Stolper, E. (1992) Water, CO_2, Cl, and F in melt inclusions in phenocrysts from three Holocene explosive eruptions, Crater Lake, Oregon. American Mineralogist, 77, 1021–1030.

Barnes, C.G., Coint, N., and Yoshinobu, A. (2016a) Crystal accumulation in a tilted arc batholith. American Mineralogist, 101, 1719–1734.

Barnes, C.G., Ernst, W.G., Berry, R., and Tsujimori, T. (2016b) Petrology and geochemistry of an upper crustal pluton: a view into crustal-scale magmatism during arc to retro-arc transition. Journal of Petrology, 1361–1388, doi: 10.1093/petrology/egw043.

Barnes, C. G., Memeti, V. and Coint, N. (2016c) Deciphering magmatic processes in calc-alkaline plutons using trace element zoning in hornblende. American Mineralogist, 101, 328–342

Beard, J. S., Ragland, P. C., and Crawford, M. L. (2005) Reactive bulk assimilation: A model for crust-mantle mixing in silicic magmas. Geology, 33, 681–684.

Berry, R.A. (2015) Hornblende as an indicator of magma batches and magmatic processes in the English Peak pluton, Klamath Mountains, California. MS thesis, Texas Tech Univ., Lubbock, 201 p.

Blundy, J. D. and Holland, T.J.B. (1990) Calcic amphibole equilibria and a new amphibole-plagioclase geothermometer. Contributions to Mineralogy and Petrology, 104, 208–224.

Boehnke, P., Watson, E.B., Trail, D., Harrison, T.M., and Schmitt, A.K. (2013) Zircon saturation re-revisited. Chemical Geology, 351, 324–334.

Challener, S.C., and Glazner, A.F. (2017) Igneous or metamorphic? Hornblende phenocrysts as greenschist facies reaction cells in the Half Dome Granodiorite, California. American Mineralogist, 102, 436–444.

Chambefort, I., Dilles, J. H. & Longo, A. A. (2013) Amphibole geochemistry of the Yanacocha volcanics, Peru: Evidence for diverse sources of magmatic volatiles related to gold ores. Journal of Petrology, 54, 1017–1046.

Chappell, B.W., White, A.J.R., and Wyborn, D. (1987) The importance of residual source material (restite) in granite petrogenesis. Journal of Petrology, 28, 1111–1138.

Cherniak, D.J. and Liang, Y. (2012) Ti diffusion in natural pyroxene. Geochimica et Cosmochimica Acta, 98, 31–47.

Claeson, D. T., Meurer, W. P., Hogmalm, K. J., and Larson, S.-Å. (2007) Using LA-ICPMS mapping and sector zonation to understand growth and trace-element partitioning in sector-zoned clinopyroxene oikocrysts from the Norra Ulvö Gabbro, Sweden. Journal of Petrology, 48, 711–728.

Clemens, J.D., Helps, P.A., and Stevens, G. (2010) Chemical structure in granitic magmas – a signal from the source? Earth and Environmental Science Transactions of the Royal Society of Edinburgh, 100, 159–172.

Coint, N., Barnes, C.G., Yoshinobu, A.S., Barnes, M.A. and Buck, S. (2013) Use of trace element abundances in augite and hornblende to determine the size, connectivity, timing, and evolution of magma batches in a tilted pluton. Geosphere, 9, 1747–1765.

Coleman, D. S., W. Gray, and Glazner, A.F. (2004) Rethinking the emplacement and evolution of zoned plutons: Geochronologic evidence for incremental assembly of the Tuolumne Intrusive Suite, California. Geology 32, 433–436.

Coleman, R.G., Mortimer, N., Donato, M.M., Manning, C.E., and Hill, L.B. (1988) Tectonic and regional metamorphic framework of the Klamath Mountains and adjacent Coast Ranges, California and Oregon. In: Ernst, W.G. (ed.) Metamorphism and Crustal Evolution of the Western United States. Prentice-Hall, Englewood Cliffs, New Jersey, 1061–1097.

Davidson, J.P., Font, L., Charlier, B.L.A., and Tepley, F.J., III. (2008) Mineral-scale Sr isotope variation in plutonic rocks – a tool for unravelling the evolution of magma systems. Transactions of the Royal Society of Edinburgh: Earth Sciences, 97, 357–367.

Davidson, J.P., Hora, J.M., Garrison, J.M., and Dungan, M.A. (2005) Crustal forensics in arc magmas. Journal of Volcanology and Geothermal Research, 140, 157–170.

Davidson, J.P., Morgan, D.J., Charlier, B.L.A., Harlou, R., and Hora, J.M. (2007) Microsampling and isotopic analysis of igneous rocks: Implications for the study of magmatic systems. Annual Review of Earth and Planetary Sciences, 35, 273–311.

Davidson, J., Tepley, F., III, Palacz, Z., and Meffan-Main, S. (2001) Magma recharge, contamination and residence times revealed by in situ laser ablation isotopic analysis of feldspar in volcanic rocks. Earth and Planetary Science Letters, 184, 427–442.

Davidson, J., Turner, S., and Plank, T. (2013) Dy/Dy*: Variations arising from mantle sources and petrogenetic processes. Journal of Petrology, 54, 525–537.

Deering, C.D., and Bachmann, O. (2010) Trace element indicators of crystal accumulation in silicic igneous rocks. Earth and Planetary Science Letters, 297, 324–331.

Deering, C.D., Bachmann, O., Dufek, J., and Gravley, D.M. (2011) Rift-related transition from andesite to rhyolite volcanism in the Taupo Volcanic Zone (New Zealand) controlled by crystal–melt dynamics in mush zones with variable mineral assemblages. Journal of Petrology, 52, 2243–2263.

Donato, M.M., Barnes, C.G., Coleman, R.G., Ernst, W.G., and Kays, M.A. (1982) Geological map of the Marble Mountain wilderness, Siskiyou County: U.S. Geological Survey Miscellaneous Field Studies Map MF-1452-A, scale 1:48 000.

Dostal, J. and Chatterjee, A. K. (2010) Lead isotope and trace element composition of K-feldspars from peraluminous granitoids of the Late Devonian South Mountain Batholith (Nova Scotia, Canada): implications for petrogenesis and tectonic reconstruction. Contributions to Mineralogy and Petrology, 159, 563–578.

Dunbar, N. W. and Hervig, R. L. (1992) Petrogenesis and volatile stratigraphy of the Bishop Tuff: Evidence from melt inclusion analysis. Journal of Geophysical Research, 97, 15129–15150.

Elburg, M., Kamenetsky, V. S., Nikogosian, I., Foden, J. and Sobolev, A. V. (2006) Coexisting high- and low-calcium melts identified by mineral and melt inclusion studies of a subduction-influenced syn-collisional magma from South Sulawesi, Indonesia. Journal of Petrology, 47, 2433–2462.

Erdmann, S., Martel, C., Pichavant, M., and Kushnir, A. (2014) Amphibole as an archivist of magmatic crystallization conditions: problems, potential, and implications for inferring magma storage prior to the paroxysmal 2010 eruption of Mount Merapi, Indonesia. Contributions to Mineralogy and Petrology, 167, http://dx.doi: 10.1007/s00410-014-1016-4.

Ernst, W.G. (1998) Geology of the Sawyers Bar area, Klamath Mountains, northern California. California Division of Mines and Geology, Map Sheet **47**, scale 1:48,000, accompanying text 59 p.

Ernst, W.G. (1999) Mesozoic petrotectonic development of the Sawyers Bar suprasubduction-zone arc, central Klamath Mountains, northern California. Geological Society of America Bulletin, 111, 1217–1232.

Ernst, W.G. and Kolodny, Y. (1997) Submarine and superimposed contact metamorphic oxygen isotopic exchange in an oceanic arc, Sawyers Bar area, central Klamath Mountains, California, USA. Geochimica et Cosmochimica Acta, 61, 821–834.

Ernst, W.G. and Liu, J. (1998) Experimental phase-equilibrium study of Al- and Ti-contents of calcic amphibole in MORB—a semiquantitative thermobarometer. American Mineralogist, 83, 952–969.

Ernst, W.G., Gottlieb, E.S., Barnes, C.G., and Hourigan, J.K. (2016) Zircon U–Pb ages and petrologic evolution of the English Peak granitic pluton: Jurassic crustal growth in northwestern California. Geosphere, 12, 1422–1436, http://dx.doi.org/10.1130/GES01340.1.

Esawi, E.K. (2004) AMPH-CLASS: An Excel spreadsheet for the classification and nomenclature of amphiboles based on the 1997 recommendations of the International Mineralogical Association. Computers & Geosciences, 30, 753–760.

Glazner, A. F., Coleman, D. S., and Bartley, J. M. (2008) The tenuous connection between high-silica rhyolites and granodiorite plutons. Geology, 36, 183–186.

Grocke, S.B., de Silva, S.L., Iriarte, R., Lindsay, J.M., and Cottrell, E. (2017) Catastrophic caldera-forming (CCF) monotonous silicic magma reservoirs: Geochemical and petrological constraints on heterogeneity, magma dynamics, and eruption dynamics of the 3.49 Ma Tara supereruption, Guacha II Caldera, SW Bolivia. Journal of Petrology.

Hacker, B.R., Ernst, W.G., and Barton, M.D. (1992) Metamorphism, geochemistry and origin of magnesian volcanic rocks, Klamath Mountains, California. Journal of metamorphic Geology, 10, 55–69.

Hammarstrom, J.M., and Zen, E. (1986) Aluminum in hornblende: An empirical igneous geobarometer. American Mineralogist, 71, 1297–1313.

Heinonen, A., Mänttäri, I., Rämö, O.T., Andersen, T., and Larjamo, K. (2016) *A priori* evidence for zircon antecryst entrainment in megacrystic Proterozoic granites. Geology, 44, 227–230.

Helz, R.T. (1982) Phase relations and compositions of amphiboles produced in studies of the melting behavior of rocks. Reviews in Mineralogy, 9B, 479–346.

Hildreth, W. (2004) Volcanological perspectives on Long Valley, Mammoth Mountain, and Mono Craters: several contiguous but discrete systems. Journal of Volcanology and Geothermal Research, 136, 169–198.

Holland, T. and Blundy, J. (1994) Non-ideal interactions in calcic amphiboles and their bearing on amphibole-plagioclase thermometry. Contributions to Mineralogy and Petrology, 116, 433–447.

Hollister, L.S., Grissom, G.C., Peters, E.K., Stowell, H.H., and Sisson, V.B. (1987) Confirmation of the empirical correlation of Al in hornblende with pressure of solidification of calc-alkaline plutons. American Mineralogist, 72, 231–239.

Kent, A. J. R. (2008) Melt inclusions in basaltic and related volcanic rocks. Reviews in Mineralogy and Geochemistry, 69, 273–331.

Klein, M., Stosch, H.-G., and Seck, H. (1997) Partitioning of high field-strength and rare-earth elements between amphibole and quartz-dioritic to tonalitic melts: an experimental study. Chemical Geology, 138, 257–271.

Kiss, B., Harangi, S., Ntaflos, T., Mason, P. R. D., and Pál-Molnár, E. (2014) Amphibole perspective to unravel pre-eruptive processes and conditions in volcanic plumbing systems beneath intermediate arc volcanoes: a case study from Ciomadul volcano (SE Carpathians). Contributions to Mineralogy and Petrology, 167.

Lackey, J.S., Valley, J.W., and Hinke, H.J. (2006) Deciphering the source and contamination history of peraluminous magmas using $\delta^{18}O$ of accessory minerals: examples from garnet-bearing plutons of the Sierra Nevada batholith. Contributions to Mineralogy and Petrology, 151, 20–44.

Leake, B., Woolley, A., Arps, C., Birch, W., Gilbert, M., Grice, J., Hawthorne, F., Kato, A., Kisch, H., Krivovichev, V., Linthout, K., Laird, J., Mandarino, J., Schumacher, J., Smith, D., Stephenson, N., Ungaretti, L., Whittaker, E., and Youzhi, G. (1997) Nomenclature of amphiboles: Report of the Subcommittee on Amphiboles of the International Mineralogical Association, Commission on New Minerals and Mineral Names. American Mineralogist, 82, 1019–1037.

Lee, C.-T.A., and Morton, D.M. (2015) High silica granites: Terminal porosity and crystal settling in shallow magma chambers. Earth and Planetary Science Letters, 409, 23–31.

Lee, C.-T.A., Morton, D.M., Farner, M.J., and Moitra, P. (2015) Field and model constraints on silicic melt segregation by compaction/hindered settling: the role of water and its effect on latent heat release. American Mineralogist, 100, 1762–1777.

Leuthold, J., Müntener, O., Baumgartner, L. P., and Putlitz, B. (2014) Petrological constraints on the recycling of mafic crystal mushes and intrusion of braided sills in the Torres del Paine mafic complex (Patagonia). Journal of Petrology, 55, 917–949.

Marks, M. A. W., Coulson, I. M., Schilling, J., Jacob, D. E., Schmitt, A. K., and Markl, G. (2008) The effect of titanite and other HFSE-rich mineral (Ti-bearing andradite, zircon, eudialyte) fractionation on the geochemical evolution of silicate melts. Chemical Geology, 257, 153–172.

Marks, M., Halama, R., Wenzel, T., and Karkl, G. (2004) Trace element variations in clinopyroxene and amphibole from alkaline to peralkaline syenites and granites: implications for mineral–melt trace-element partitioning. Chemical Geology, 211, 185–215.

Mattinson, J.M. (2005) Zircon U–Pb chemical abrasion ("CA-TIMS") method: Combined annealing and multi-step partial dissolution analysis for improved precision and accuracy of zircon ages. Chemical Geology, 220, 47–66.

Matzel, J.E.P., Bowring, S.A., and Miller, R.B. (2006) Time scales of pluton construction at differing crustal levels: Examples from the Mount Stuart and Tenpeak intrusions, North Cascades, Washington. Geological Society of America Bulletin, 118, 1412–1430.

McLeod, G. W., Dempster, T. J., and Faithfull, J. W. (2011) Deciphering magma-mixing processes using zoned titanite from the Ross of Mull granite, Scotland. Journal of Petrology, 52, 55–82.

Memeti, V., Paterson, S., Matzel, J., Mundil, R., and Okaya, D. (2010) Magmatic lobes as "snapshots" of magma chamber growth and evolution in large, composite batholiths: An example from the Tuolumne intrusion, Sierra Nevada, California. Geological Society of America Bulletin, 122, 1912–1931.

Michel, J., Baumgartner, L., Putlitz, B., Schaltegger, U., and Ovtcharova, M. (2008) Incremental growth of the Patagonian Torres del Paine laccolith over 90 k.y. Geology, 36, 459–462.

Miller, C.F., Furbish, D.J., Walker, B.A., Claiborne, L.L., Koteas, G.C., Bleick, H.A., and Miller, J.S. (2011) Growth of plutons by incremental emplacement of sheets in crystal-rich host: Evidence from Miocene intrusions of the Colorado River region, Nevada, USA. Tectonophysics, 500, 65–77.

Moore, J. G. and Sisson, T. W. (2008) Igneous phenocrystic origin of K-feldspar megacrysts in granitic rocks from the Sierra Nevada batholith. Geosphere, 4, 387–400.

Müller, A., Breiter, K., Seltmann, R., and Pécskay, Z. (2005) Quartz and feldspar zoning in the eastern Erzgebirge volcano-plutonic complex (Germany, Czech Republic): evidence of multiple magma mixing. Lithos, 80, 201–227.

Nandedkar, R. H., Hürllmann. N., Ulmer, P., and Müntener, O. (2016) Amphibole–melt trace element partitioning of fractionating calc-alkaline magmas in the lower crust: an experimental study. Contributions to Mineralogy and Petrology, 171, http://dx.doi.org/10.1007/s00410-016-1278-0.

Otamendi, J.E., Tiepolo, M., Walker, B.A., Jr., Cristofolini, E.A., and Tibaldi, A.M. (2016) Trace elements in minerals from mafic and ultramafic cumulates of the central Sierra de Valle Fértil, Famatinian arc, Argentina. Lithos, 240–243.

Pe-Piper, G. (1988) Calcic amphiboles of mafic rocks of the Jeffers Brook plutonic complex, Nova Scotia, Canada. American Mineralogist, 73, 993–1006.

Putirka, K. (2016) Amphibole thermometers and barometers for igneous systems, and some implications for eruption mechanisms of felsic magmas at arc volcanoes. American Mineralogist, 101, 841–858.

Saunders, K. E., Baker, J. A., and Wysoczanski, R. J. (2010) Microanalysis of large volume silicic magma in continental and oceanic arcs: Melt inclusions in Taupo Volcanic zone and

Kermadec Arc rocks, South West Pacific. Journal of Volcanology and Geothermal Research, 190, 203–218.

Schaltegger, U., Brack, P., Ovtcharova, M., Peytcheva, I., Schoene, B., Stracke, A., Marocchi, M., and Bargossi, G.M. (2009) Zircon and titanite recording 1.5 million years of magma accretion, crystallization and initial cooling in a composite pluton (southern Adamello batholith, northern Italy). Earth and Planetary Science Letters, 286, 208–218.

Scherer, H. H., Ernst, W. G., and Wooden, J. L. (2010) Regional detrital zircon provenance of exotic metasandstone blocks, Eastern Hayfork terrane, Western Paleozoic and Triassic belt, Klamath Mountains, California. Journal of Geology, 118, 641–653.

Schmidt, B. L. (1994) The petrology and geochemistry of the English Peak intrusive suite, Klamath Mountains, California [Ph.D. dissertation]: Lubbock, Texas Tech University, 216 p.

Schmidt, M.W. (1992) Amphibole composition in tonalite as a function of pressure: an experimental calibration of the Al-in-hornblende barometer. Contributions to Mineralogy and Petrology, 110, 304–310.

Schoene, B., Latkoczy, C., Schaltegger, U., and Günther, D. (2010) A new method integrating high-precision U–Pb geochronology with zircon trace element analysis (U–Pb TIMS-TEA). Geochimica et Cosmochimica Acta, 74, 7144–7159.

Schoene, B., Schaltegger, U., Brack, P., Latkoczy, C., Stracke, A., and Günther, D. (2012) Rates of magma differentiation and emplacement in a ballooning pluton recorded by U–Pb TIMS-TEA, Adamello batholith, Italy. Earth and Planetary Science Letters, 355–356, 162–173.

Seyfert, C., Jr. (1965) Geology of the Sawyers Bar area, Klamath Mountains, northern California [Ph.D. dissertation]: Stanford, California, Stanford University, 227 p.

Shaw, D.M. (2006) Trace elements in magmas, a theoretical treatment. Cambridge University Press, Cambridge, U.K., 243p.

Shaw, S. E. & Flood, R. H. (2009) Zircon Hf isotopic evidence for mixing of crustal and silicic mantle-derived magmas in a zoned granite pluton, eastern Australia. Journal of Petrology 50, 147–168.

Shane, P. & Smith, V. C. (2013). Using amphibole crystals to reconstruct magma storage temperatures and pressures for the post-caldera collapse volcanism at Okataina volcano. Lithos 156–159, 159–170.

Shimizu, K., Liang, Y., Sun, C., Jackson, C.R.M. and Saal, A.E. (in press). Parameterized lattice strain models for REE partitioning between amphibole and silicate melt. American Mineralogist.

Stephens, W. (2001) Polycrystalline amphibole aggregates (clots) in granites as potential I-type restite: an ion microprobe study of rare-earth distributions. Australian Journal of Earth Sciences, 48, 591–601.

Tappa, M.J., Coleman, D.S., Mills, R.D., and Samperton, K.M. (2011) The plutonic record of a silicic ignimbrite from the Latir volcanic field, New Mexico. Geochemistry Geophysics Geosystems, 12(10).

Tiepolo, M., Oberti, R., Zanetti, A., Vannucci, R., and Foley, S.F. (2007) Trace-element partitioning between amphibole and silicate melt. Reviews in Mineralogy & Geochemistry, 67, 417–452.

Turner, S. J., Izbekov, P., and Langmuir, C. (2013) The magma plumbing system of Bezymianny Volcano: Insights from a 54 year time series of trace element whole-rock geochemistry and amphibole compositions. Journal of Volcanology and Geothermal Research, 10.1016/j.volgeores.2012.12.014.

Vogel, T. A. and Aines, R. (1996) Melt inclusions from chemically zoned ash flow sheets from the southwest Nevada volcanic field. Journal of Geophysical Research, 101, 5591–5610.

Waight, T., Mass, R., and Nicholls, I. (2000) Fingerprinting feldspar phenocrysts using crystal isotopic composition stratigraphy: implications for crystal transfer and magma mingling in S-type granites. Contributions to Mineralogy and Petrology, 139, 227–239.

Watson, E.B. and Harrison, T.M. (1983) Zircon saturation revisited: temperature and composition effects in a variety of crustal magma types. Earth and Planetary Science Letters, 64, 295–304.

White, A.J.R., and Chappell, B.W. (1977) Ultrametamorphism and granitoid genesis. Tectonophysics, 43, 7–22.

Whitney, D.L., and Evans, B.W. (2010) Abbreviations for names of rock-forming minerals. American Mineralogist, 95, 185–187.

Wright, J. E. (1982) Permo-Triassic accretionary subduction complex, southwestern Klamath Mountains, northern California. Journal of Geophysical Research, 87, 3805–3818.

Zhang, J., Davidson, J.P., Humphreys, M.C.S., Macpherson, C.G., and Neill, I. (2015) Magmatic enclaves and andesitic lavas from Mt. Lamington, Papua New Guinea: Implications for recycling of earlier-fractionated minerals through magma recharge. Journal of Petrology, 56, 2223–2256.

Zhang, J., Humphreys, M.C.S., Cooper, G.F., Davidson, J.P., and Macpherson, C.G. (2017) Magma mush chemistry at subduction zones, revealed by new melt major element inversion from calcic amphiboles. American Mineralogist, 102, 1353–1367.

Figure Captions.

Figure 1. Generalized geologic map of the English Peak plutonic complex, after Ernst (1998) and Barnes et al. (2016b) with NAD27 UTM grid. Analyzed samples from the late stage of the English Peak pluton are indicated by black symbols. Green symbols indicate samples from older units of the complex (Berry, 2015). The inset shows the location of the study area within the Klamath Mountain province.

Figure 2. Photomicrographs are all in plane-polarized light. Letters indicate locations of laser-ablation pits and temperature values are those calculated for individual spots using the thermometer of Putirka (2016). A. Hornblende from YJR unit, sample EP-176B, showing olive-brown core rimmed and embayed by green hornblende. Note biotite inclusions associated with embayed zones and local inclusion trains of minute accessory apatite and ilmenite. Ablation pits are 40 µm in diameter. B. Hornblende from CR unit, sample RBEP-022, with wide green rims. Note accessory allanite in contact with green hornblende. C. Hornblende from YJR unit, sample EP-219, with deeply embayed core and widespread deuteric chlorite. D. Inclusions of ilmenite and zircon in the olive-brown core of hornblende from YJR sample EP-176B. E. Inclusions of zircon in YJR sample EP-216. F. Hornblende from northern border unit, sample RBEP-021. Note the paucity of olive-brown hornblende (minor spots in crystal 8) and the uniform green color of the remainder of the crystals. G. Compositional transect across the near-vertical boundary between olive-green core and green embayed zone. Data are counts for Mg and Al using 5 ms dwell time.

This is a preprint, the final version is subject to change, of the American Mineralogist (MSA)
Cite as Authors (Year) Title. American Mineralogist, in press.
(DOI will not work until issue is live.) DOI: http://dx.doi.org/10.2138/am-2017-6063

Figure 3. Hornblende major element compositions. In all panels, the gray line separates compositions of olive-brown cores from green rims and actinolite. In panels B–D, field represent compositional ranges of amphibole from caldera-forming eruptions of the Fish Canyon Tuff (Bachmann and Dungan, 2002), the Okataina eruptions in the Taupo center (Deering et al., 2011; Shane and Smith, 2013), and the Guacha II caldera (Grocke et al.2017). A. $Mg/(Mg+Fe_{total})$ vs. Si (atoms per formula unit = apfu). Classification of Leake et al. (1997). B. Na vs. Si. Note the increase in Na from border unit to Chimney Rock unit. C. Ti vs. Si. Amphibole classified as actinolite typically has Ti contents less than 0.07 apfu. D. Mn vs. Si. The outer cores and green rims of Chimney Rock hornblende have distinctly higher Mn than hornblende from the border or Yellow Jacket Ridge units. One exception is sample RBEP-021 from the northern border unit, with notably higher Mn than other border unit hornblende.

Figure 4. Hornblende trace element compositions. In all panels, the gray line separates compositions of olive-brown cores from green rims. Note the distinct compositional trends for sample RBEP-021 from the northern border unit in terms of Eu, Sc, Y, Sm, Yb, Eu/Eu*, and normalized La/Lu ratio (La_N/Lu_N). See text for further discussion. The small cross indicates typical 1σ analytical precision.

Figure 5. Representative REE diagrams normalized to chondritic values (Anders and Grevesse [1989] values multiplied by 1.36). In all panels, circles represent analyses of the interiors of olive-brown cores, inverted triangles represent analyses of the outer parts of olive-brown cores, triangles represent analyses of green embayed zones, and squares represent green rims. Temperature ranges are for olive-brown cores versus green embayed zones and rims. A. Individual patterns are plotted for hornblende from border unit sample EP-121. The field

Always consult and cite the final, published document. See http:/www.minsocam.org or GeoscienceWorld

represents hornblende compositions for sample RBEP-021 in which nearly all crystals lack olive-brown zones. B and C. Examples of hornblende from the Yellow Jacket Ridge unit. D. and E. Examples of hornblende from the Chimney Rock unit. Note the flattening of the REE pattern among rims. F. REE pattern of allanite from Chimney Rock sample RBEP-022.

Figure 6. Variation of temperature as a function of Ti. The gray line separates core and rim compositions. Fields of volcanic Hbl compositions as in Figure 3.

Figure 7. Schematic illustration of trace element zoning in hornblende and its relationship to core–rim boundaries, Zr content, and hornblende crystallization temperature.

Figure 8. Fractional crystallization and resorption models for trace element variation in hornblende. See text and Supplementary Data 3 for discussion.

Figure 9. A. Variation in calculated Zr contents of melts in equilibrium with Hbl depending on the choice of $d_{Hbl/melt}$ value. The left axis represents a $d_{Hbl/melt}$ for Zr of 0.68 (Klein et al., 1997) and the right axis a $d_{Hbl/melt}$ of 1.0 Nandedkar et al. (2016). T was calculated after Putirka (2016). The range of bulk-rock Zr contents for late-stage samples (Barnes et al., 2016b) is shown as a gray bar on each y-axis. Black bars along the top of the diagram indicate the range of zircon saturation temperatures assuming bulk rock compositions represent melt compositions; ‘B’ indicates the calibration of Boehnke et al. 2013) and W&H indicates the calibration of Watson and Harrison (1983). The red bar represents the combined range of Ti-in-zircon temperatures for one YJR and one CR sample (unpublished zircon analyses, K. Werts and C. Barnes).

Figure 10. Calculated REE contents of melts in equilibrium in equilibrium with representative Hbl. Melt compositions in equilibrium with olive-brown cores were calculated using $d_{Hbl/melt}$ from Klein et al. (1997; olive pattern) and Nandedkar et al. (2016; blue pattern, using 830°C $d_{Hbl/melt}$ values). Melts in equilibrium with green rims were calculated using $d_{Hbl/melt}$ values from Klein et al. (1997). Bulk-rock REE patterns are plotted as individual patterns.

Figure 11. A. Schematic view of the middle- to upper-crustal architecture of the English Peak magmatic system, after Barnes et al. (2016b) and Ernst et al. (2016). Late-stage units are: border unit (yellow), Yellow Jacket Ridge unit (pink) and Chimney Rock unit (purple). B. Photomicrograph of a euhedral olive-brown hornblende from the upper mid-crustal magma reservoir. C. Photomicrograph of Hbl typical of the YJR unit. Resorption was associated with rise of the magma to the level of emplacement and was followed by infilling of embayments and crystallization of euhedral rims by green Hbl. D. Photomicrograph of Hbl common in the CR unit, with greater resorption of the olive-brown core followed by crystallization of subhedral green rim.

This is a preprint, the final version is subject to change, of the American Mineralogist (MSA)
Cite as Authors (Year) Title. American Mineralogist, in press.
(DOI will not work until issue is live.) DOI: http://dx.doi.org/10.2138/am-2017-6063

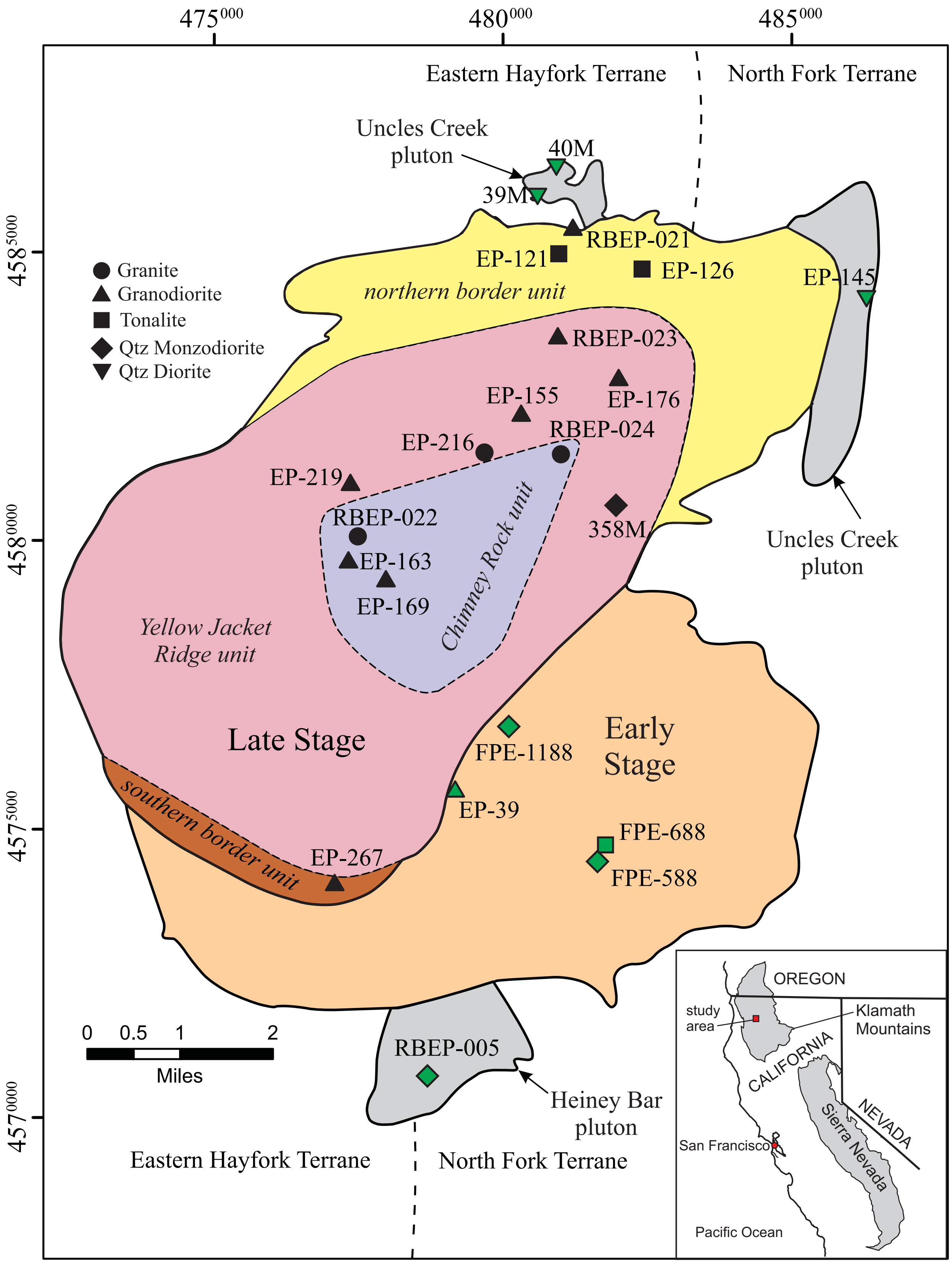

Figure 1

Always consult and cite the final, published document. See http:/www.minsocam.org or GeoscienceWorld

This is a preprint, the final version is subject to change, of the American Mineralogist (MSA)
Cite as Authors (Year) Title. American Mineralogist, in press.
(DOI will not work until issue is live.) DOI: http://dx.doi.org/10.2138/am-2017-6063

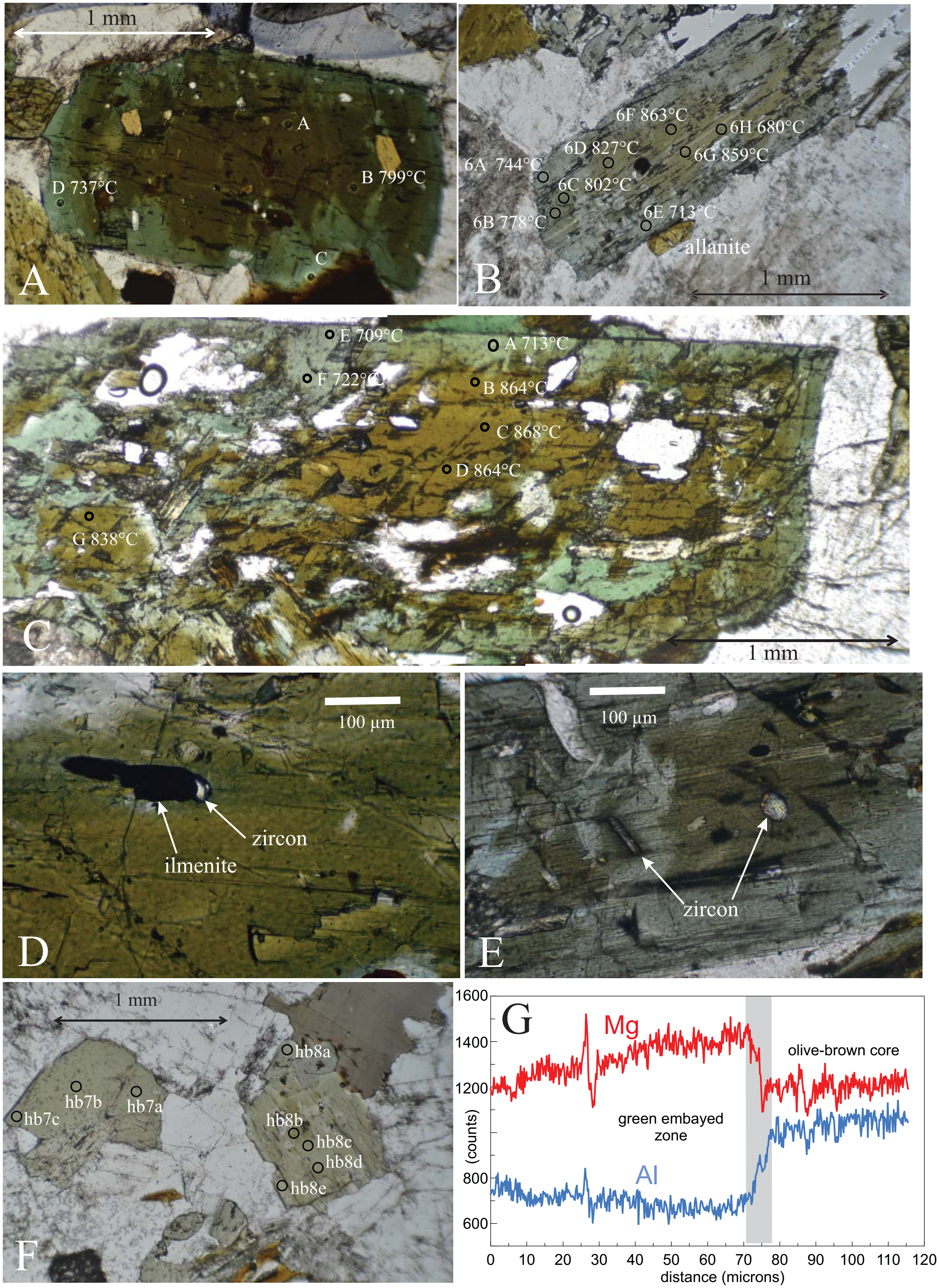

Figure 2

Always consult and cite the final, published document. See http:/www.minsocam.org or GeoscienceWorld

This is a preprint, the final version is subject to change, of the American Mineralogist (MSA)
Cite as Authors (Year) Title. American Mineralogist, in press.
(DOI will not work until issue is live.) DOI: http://dx.doi.org/10.2138/am-2017-6063

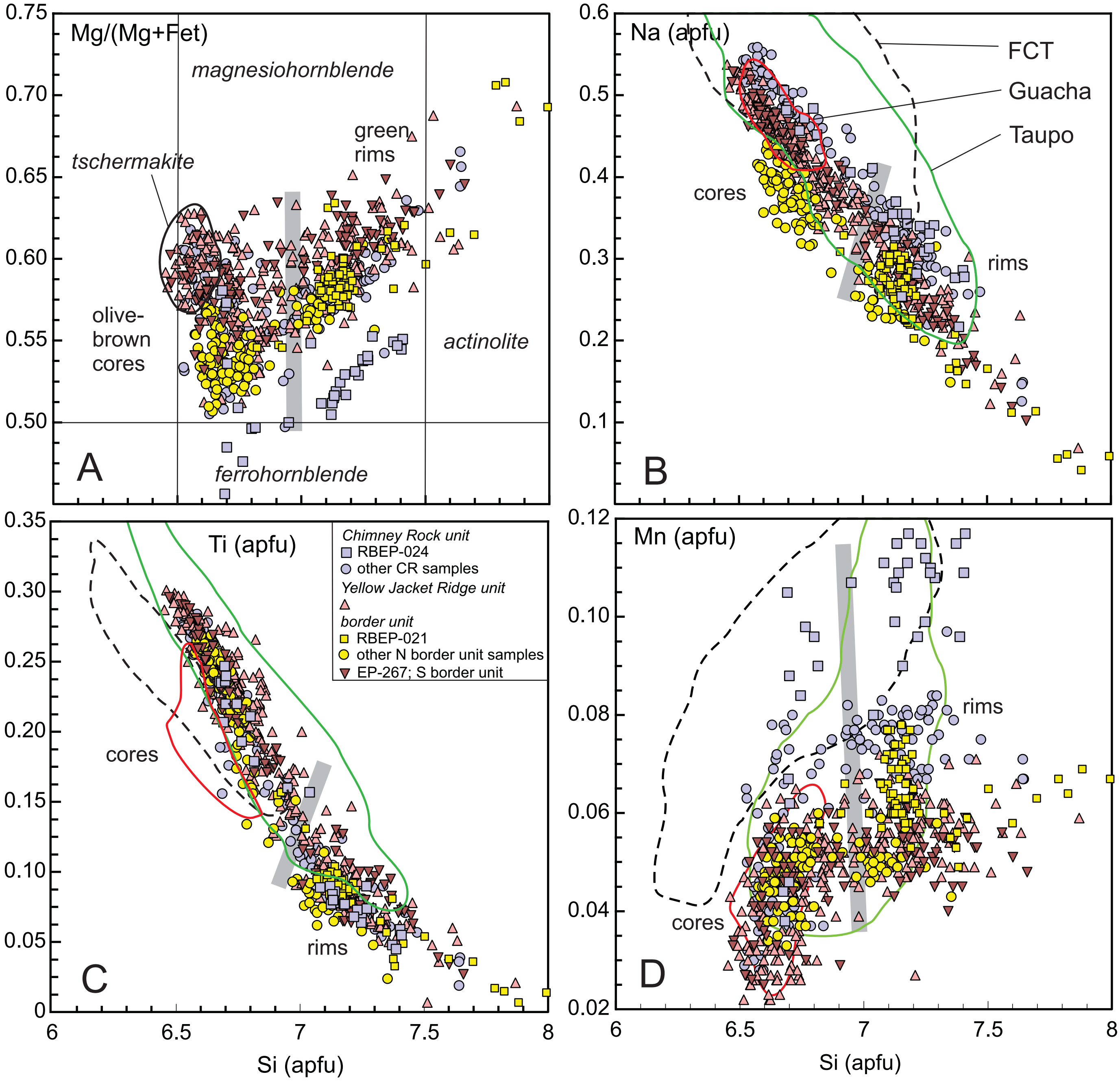

Figure 3

Always consult and cite the final, published document. See http:/www.minsocam.org or GeoscienceWorld

This is a preprint, the final version is subject to change, of the American Mineralogist (MSA)
Cite as Authors (Year) Title. American Mineralogist, in press.
(DOI will not work until issue is live.) DOI: http://dx.doi.org/10.2138/am-2017-6063

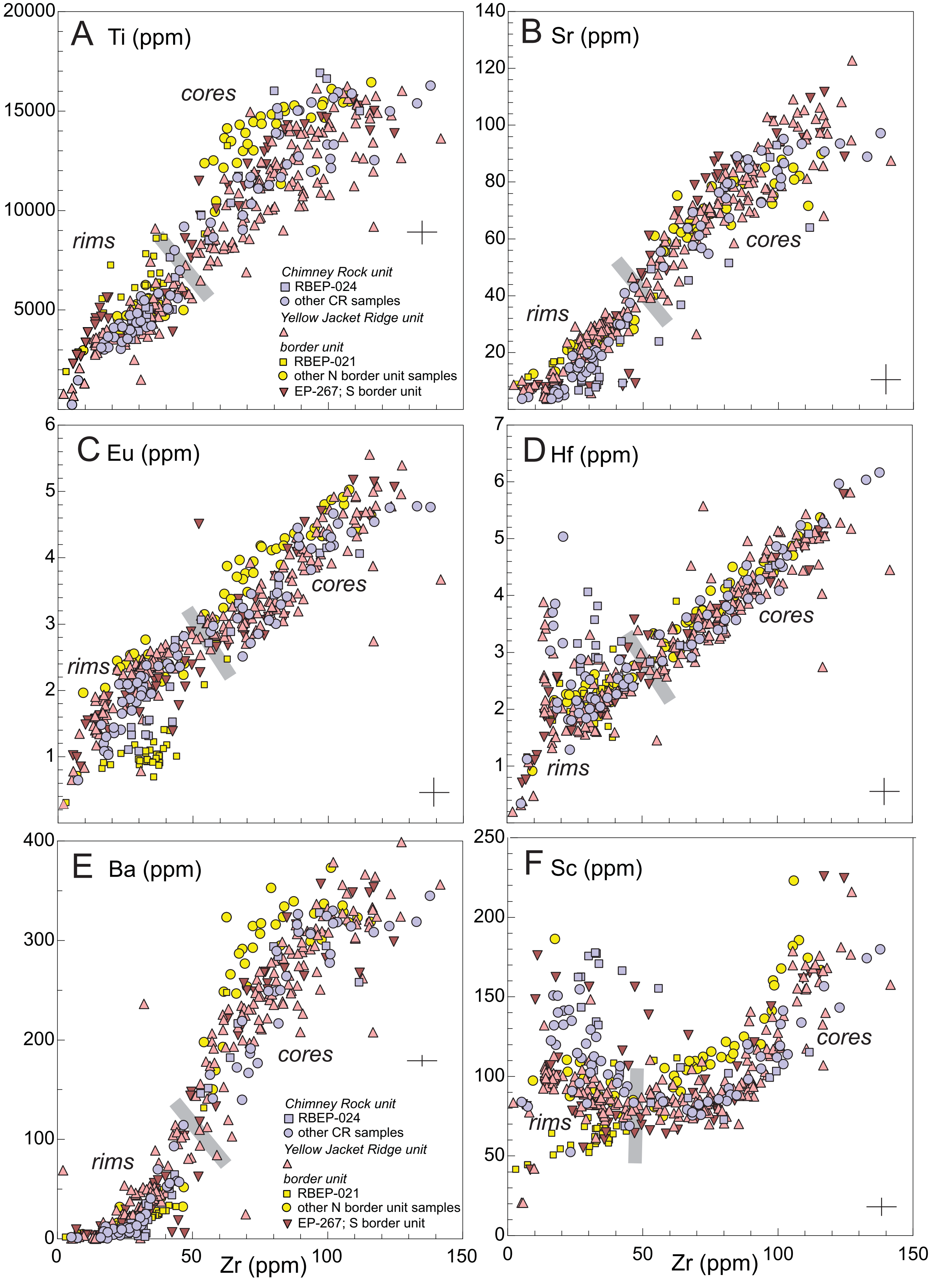

Figure 4, part 1

Always consult and cite the final, published document. See http:/www.minsocam.org or GeoscienceWorld

This is a preprint, the final version is subject to change, of the American Mineralogist (MSA)
Cite as Authors (Year) Title. American Mineralogist, in press.
(DOI will not work until issue is live.) DOI: http://dx.doi.org/10.2138/am-2017-6063

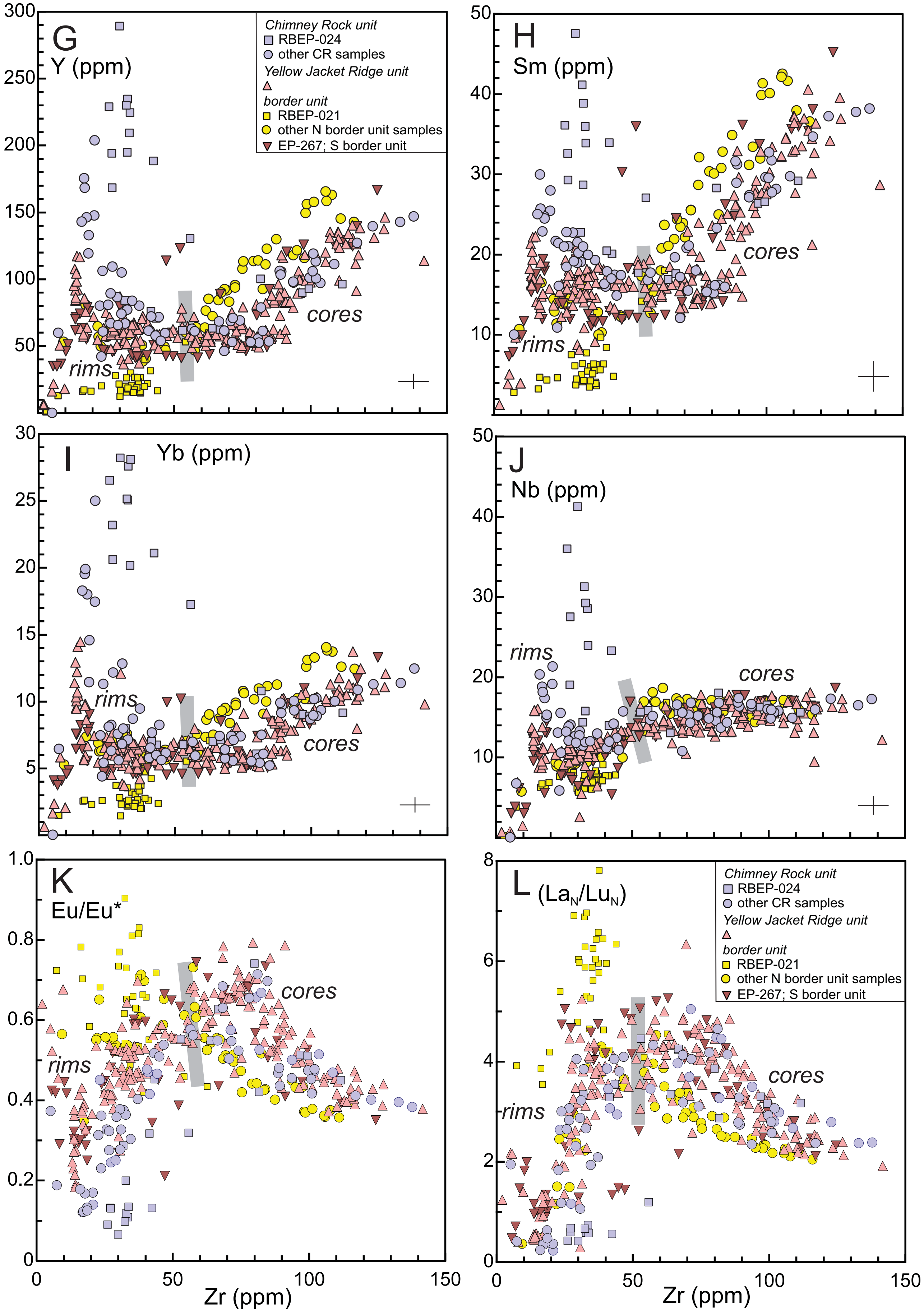

Figure 4, part 2

Always consult and cite the final, published document. See http:/www.minsocam.org or GeoscienceWorld

This is a preprint, the final version is subject to change, of the American Mineralogist (MSA)
Cite as Authors (Year) Title. American Mineralogist, in press.
(DOI will not work until issue is live.) DOI: http://dx.doi.org/10.2138/am-2017-6063

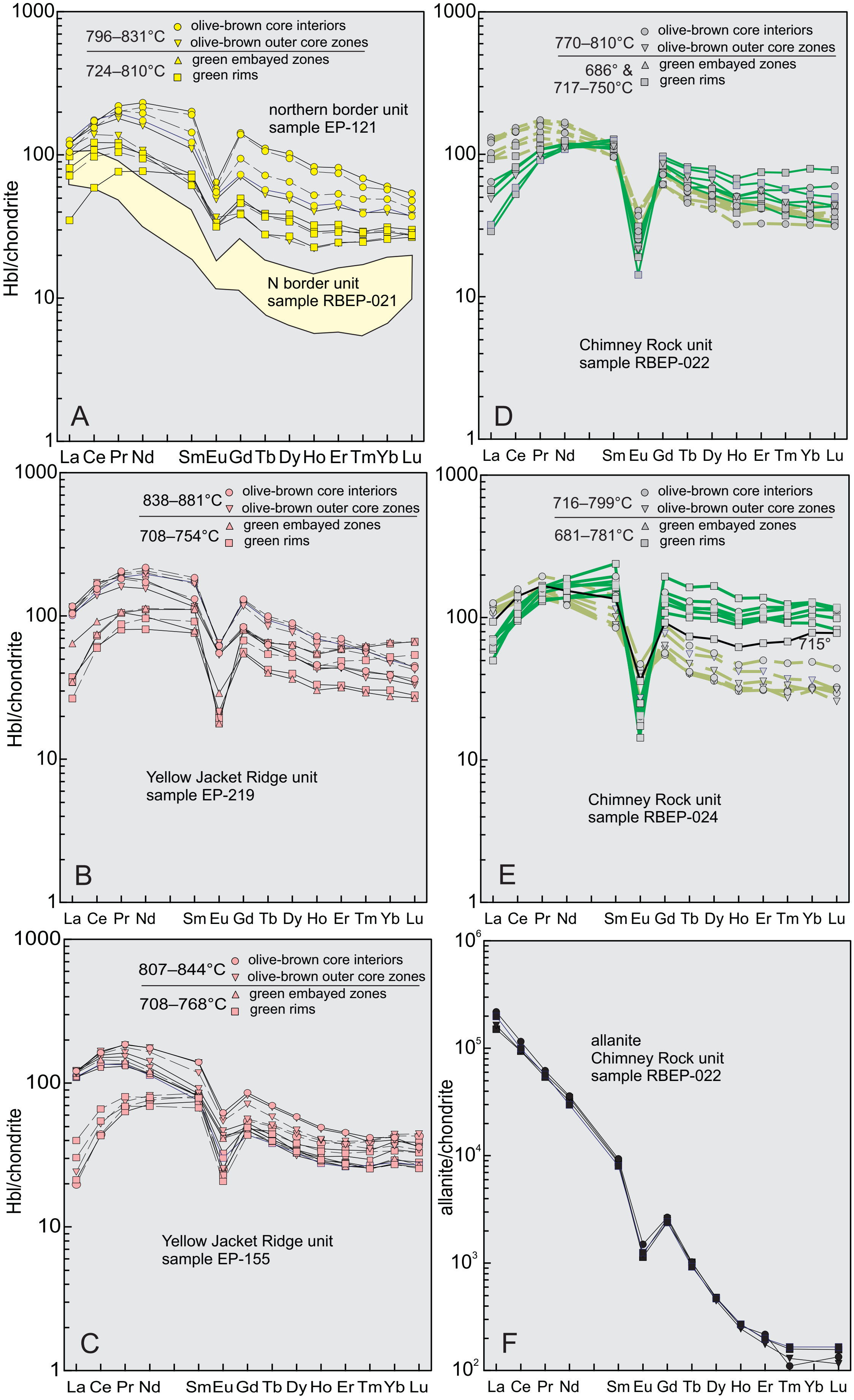

Figure 5

Always consult and cite the final, published document. See http:/www.minsocam.org or GeoscienceWorld

This is a preprint, the final version is subject to change, of the American Mineralogist (MSA)
Cite as Authors (Year) Title. American Mineralogist, in press.
(DOI will not work until issue is live.) DOI: http://dx.doi.org/10.2138/am-2017-6063

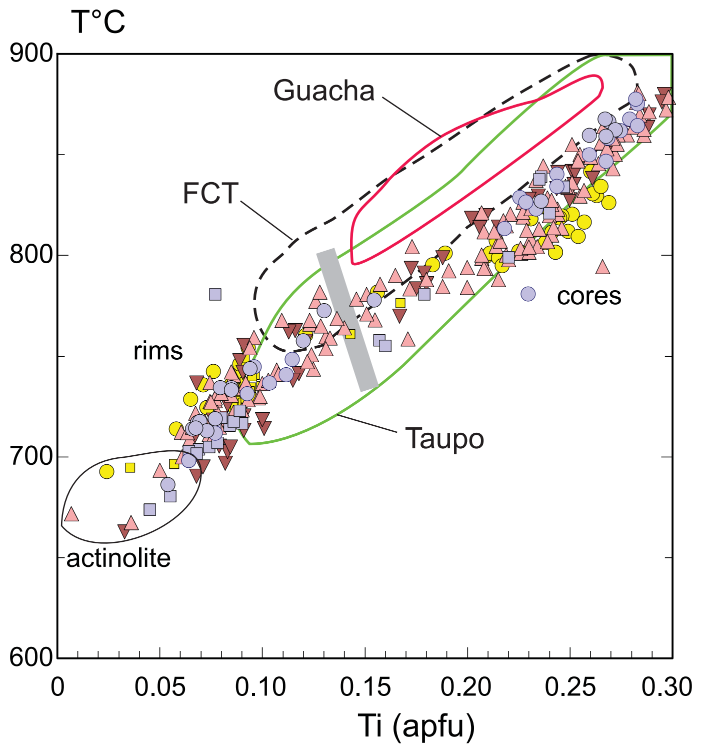

Figure 6

Always consult and cite the final, published document. See http:/www.minsocam.org or GeoscienceWorld

This is a preprint, the final version is subject to change, of the American Mineralogist (MSA)
Cite as Authors (Year) Title. American Mineralogist, in press.
(DOI will not work until issue is live.) DOI: http://dx.doi.org/10.2138/am-2017-6063

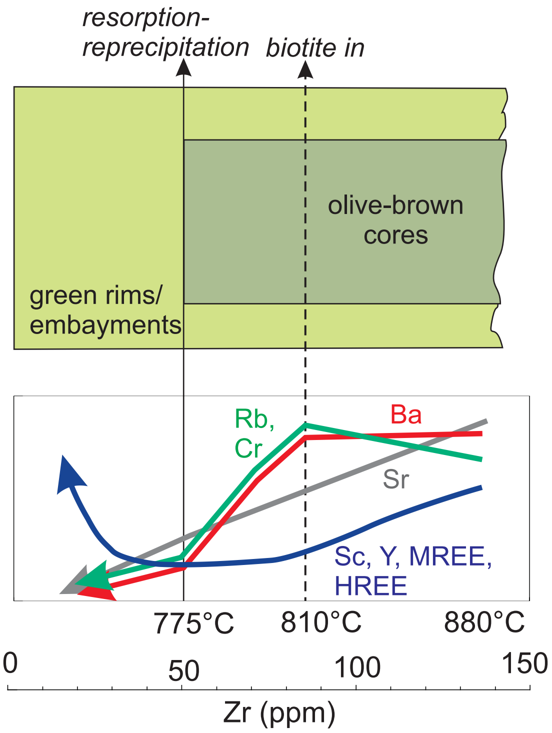

Figure 7

Always consult and cite the final, published document. See http:/www.minsocam.org or GeoscienceWorld

This is a preprint, the final version is subject to change, of the American Mineralogist (MSA)
Cite as Authors (Year) Title. American Mineralogist, in press.
(DOI will not work until issue is live.) DOI: http://dx.doi.org/10.2138/am-2017-6063

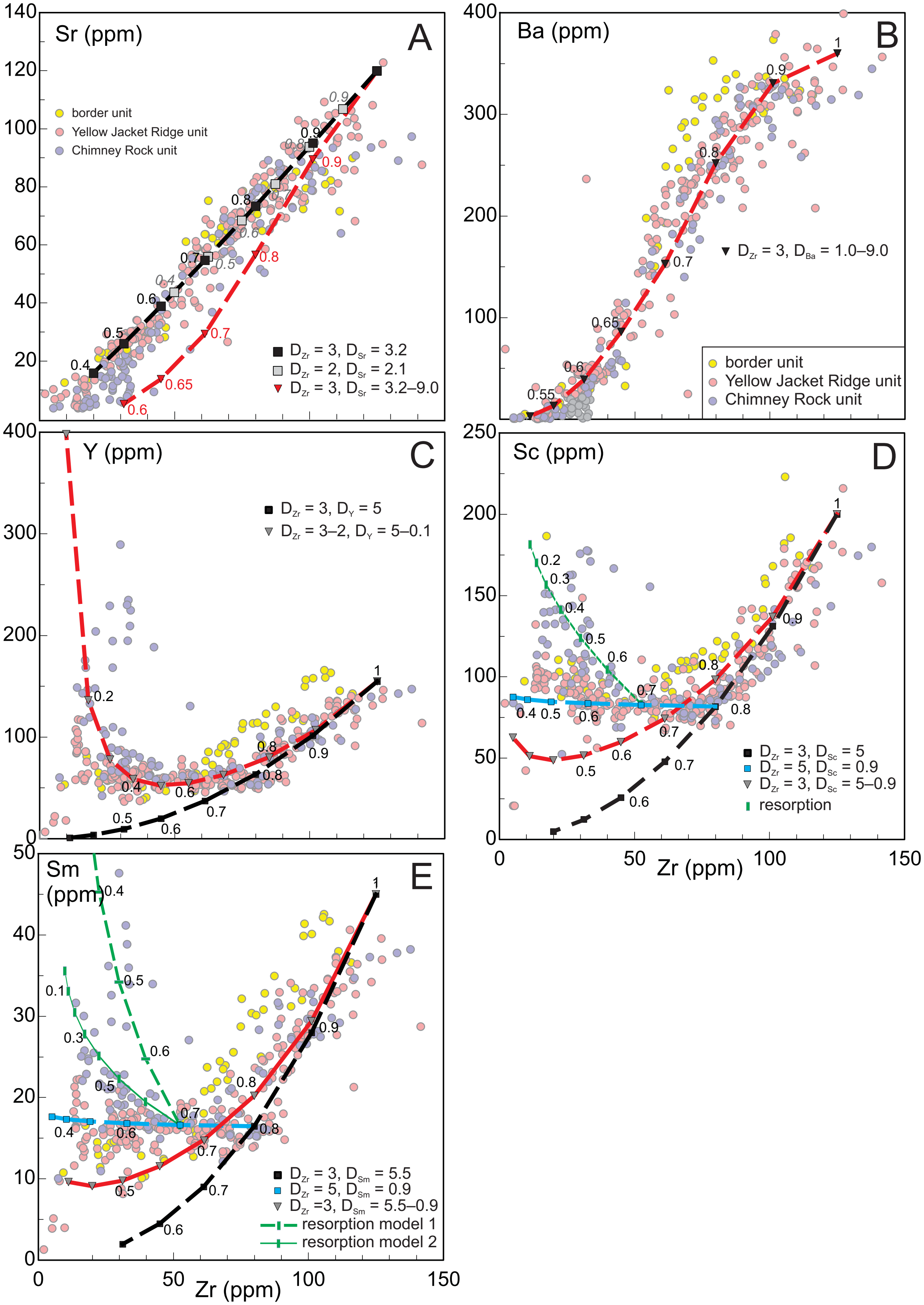

Figure 8

Always consult and cite the final, published document. See http:/www.minsocam.org or GeoscienceWorld

This is a preprint, the final version is subject to change, of the American Mineralogist (MSA)
Cite as Authors (Year) Title. American Mineralogist, in press.
(DOI will not work until issue is live.) DOI: http://dx.doi.org/10.2138/am-2017-6063

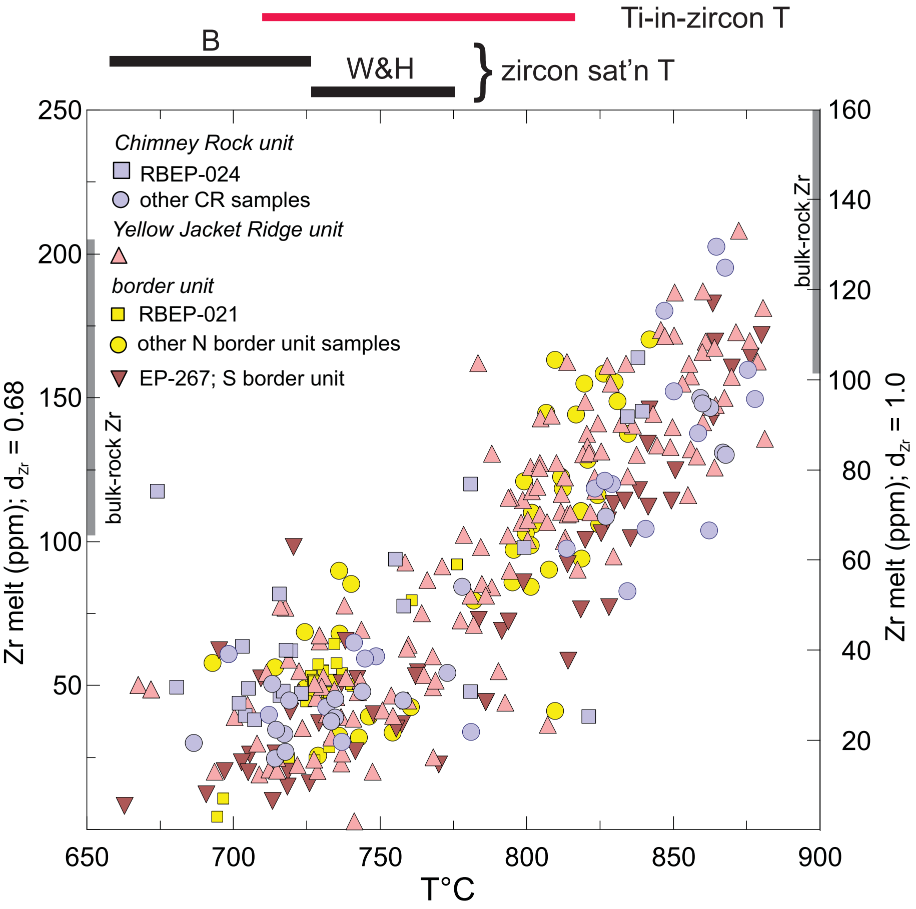

Figure 9

Always consult and cite the final, published document. See http:/www.minsocam.org or GeoscienceWorld

This is a preprint, the final version is subject to change, of the American Mineralogist (MSA)
Cite as Authors (Year) Title. American Mineralogist, in press.
(DOI will not work until issue is live.) DOI: http://dx.doi.org/10.2138/am-2017-6063

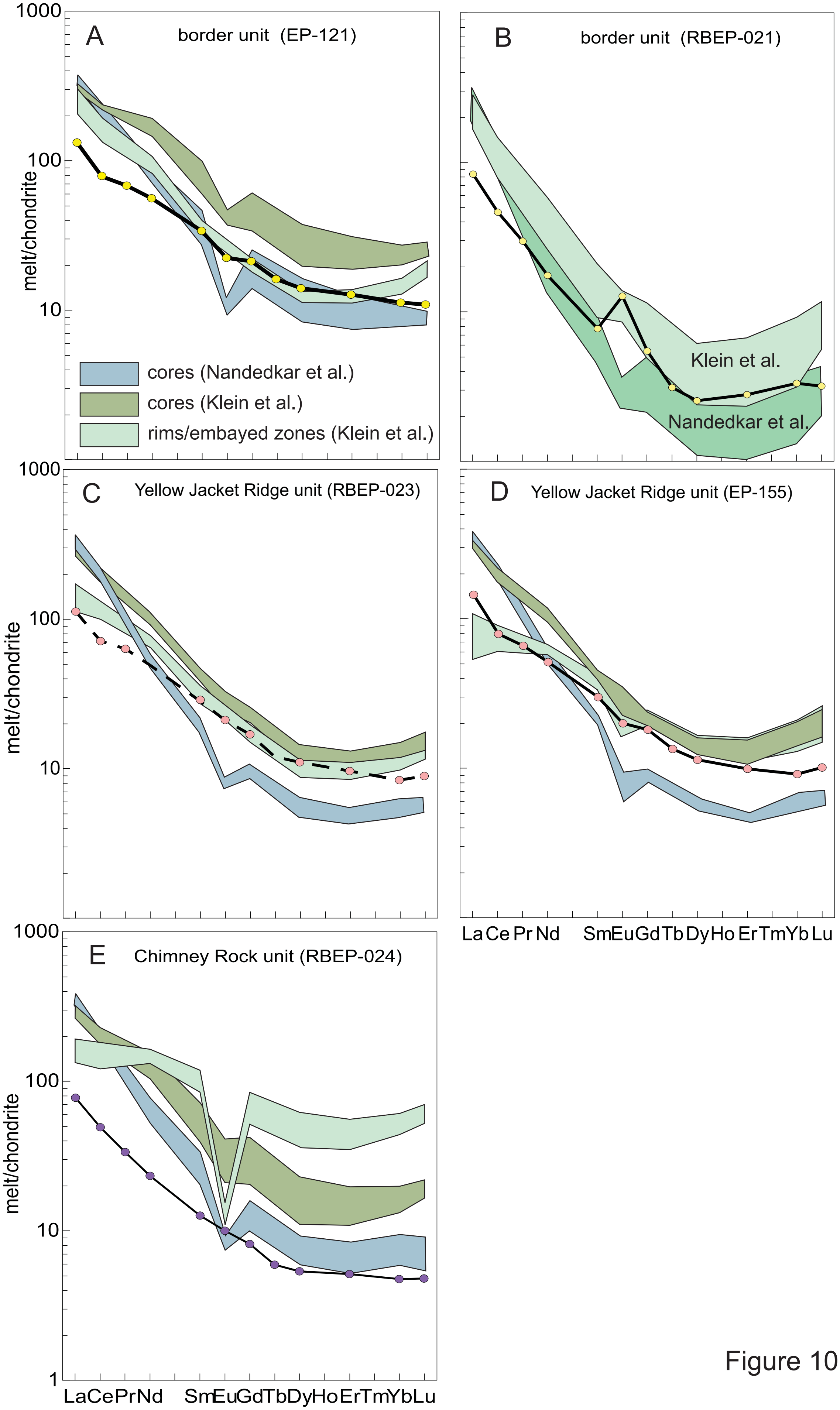

Figure 10

Always consult and cite the final, published document. See http:/www.minsocam.org or GeoscienceWorld

This is a preprint, the final version is subject to change, of the American Mineralogist (MSA)
Cite as Authors (Year) Title. American Mineralogist, in press.
(DOI will not work until issue is live.) DOI: http://dx.doi.org/10.2138/am-2017-6063

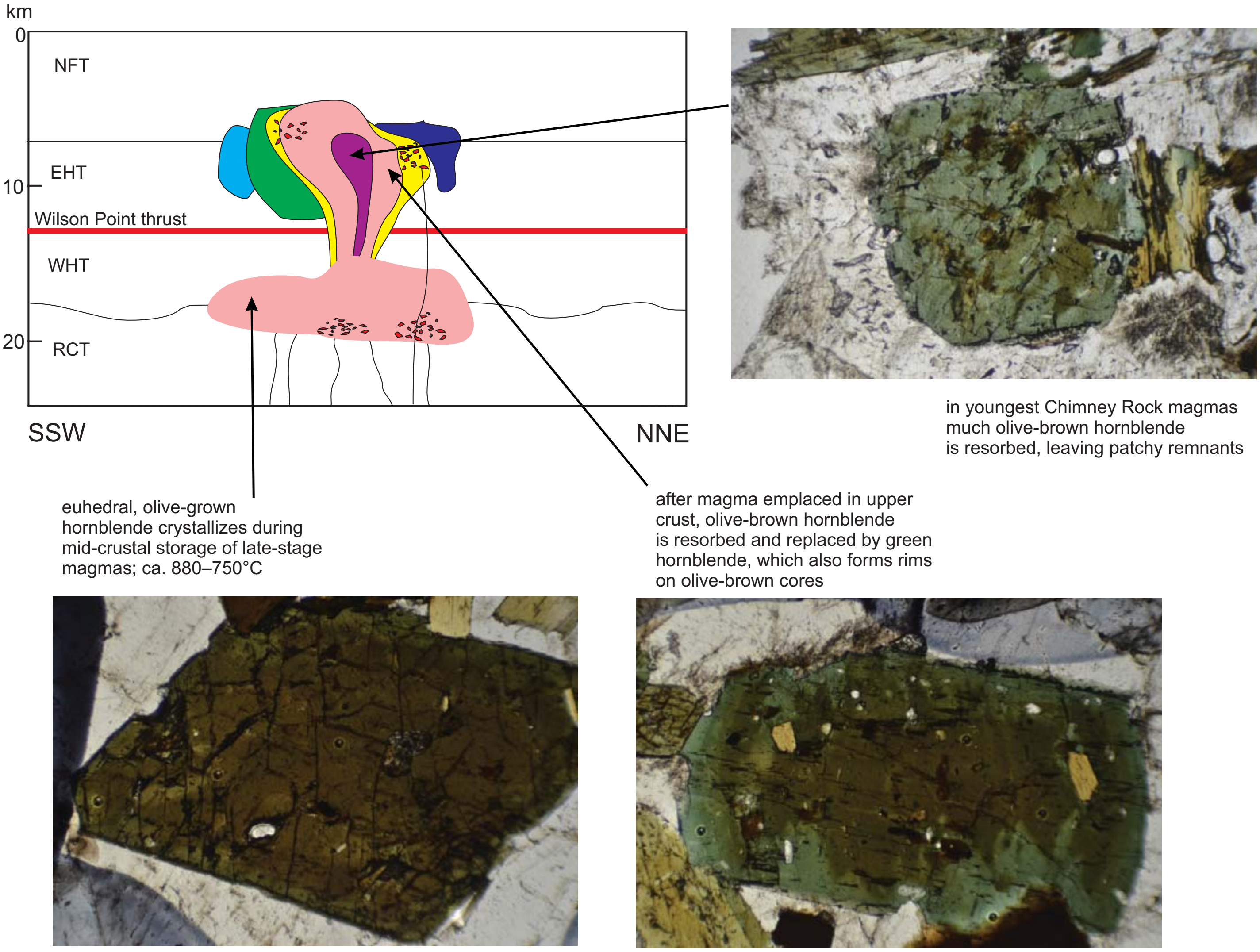

in youngest Chimney Rock magmas much olive-brown hornblende is resorbed, leaving patchy remnants

euhedral, olive-grown hornblende crystallizes during mid-crustal storage of late-stage magmas; ca. 880–750°C

after magma emplaced in upper crust, olive-brown hornblende is resorbed and replaced by green hornblende, which also forms rims on olive-brown cores

Figure 11

Always consult and cite the final, published document. See http:/www.minsocam.org or GeoscienceWorld